

Article

Coastal Depositional Responses to Relative Sea-Level Rise: Insights from a Superimposed Sandstone–Shale–Coal Reservoir in the Linxing Gas Field, China

Jincheng Liu ¹ , Yan Zhang ²  and Jingqiang Tan ^{1,*}

- ¹ Key Laboratory of Metallogenic Prediction of Nonferrous Metals and Geological Environment Monitoring, Ministry of Education, School of Geosciences and Info-Physics, Central South University, Changsha 410083, China; liujincheng@csu.edu.cn
- ² Research Institute of Petroleum Exploration and Development, PetroChina, Beijing 100083, China; zhangycugb@163.com
- * Correspondence: tanjingqiang@aliyun.com

Abstract: The Ximing Sandstone-to-No. 9 Coal succession of the Taiyuan Formation in the Linxing gas field records a complex internal architecture of a transgressive succession developed in the western coast of the late Pennsylvanian North China epeiric sea. Facies and sequence stratigraphic analyses reveal its depositional evolution from fluvial channels through fluvial-dominated and tide-influenced inner estuaries to tide-dominated estuaries and finally to wave-dominated barrier lagoons. The evolution from fluvial- to tide-dominated deposition has been ascribed to the funnel-shaped valley coupled with an increased tidal prism induced by the upstepping and backstepping shoreline. The evolution from tide- to wave-dominated deposition has been ascribed to the wide North China epeiric seaway lacking local coastline irregularities after the incised-valley fill that provided sufficient fetch for the occurrence of large storm waves. Grain-size analysis reveals the relative importance of traction, saltation, dispersed suspension, and flocculated suspension in the development of the transgressive estuarine to lagoonal deposits. This study not only contributes to a proper understanding of coastal depositional response to the relative sea-level rise but also provides a context within which to interpret the symbiotic relationship of the superimposed sandstone–shale–coal reservoirs and predict the distribution of favorable unconventional gas production formation.

Keywords: Linxing gas field; Taiyuan formation; superimposed gas reservoirs; symbiotic relationship; coastal evolution; depositional processes



Citation: Liu, J.; Zhang, Y.; Tan, J. Coastal Depositional Responses to Relative Sea-Level Rise: Insights from a Superimposed Sandstone–Shale–Coal Reservoir in the Linxing Gas Field, China. *Energies* **2023**, *16*, 4144. <https://doi.org/10.3390/en16104144>

Academic Editor: Reza Rezaee

Received: 29 April 2023

Revised: 7 May 2023

Accepted: 11 May 2023

Published: 17 May 2023



Copyright: © 2023 by the authors. Licensee MDPI, Basel, Switzerland. This article is an open access article distributed under the terms and conditions of the Creative Commons Attribution (CC BY) license (<https://creativecommons.org/licenses/by/4.0/>).

1. Introduction

Coastal evolution refers to the mutual adjustment of morphodynamic (i.e., migration of geomorphic units) and hydrodynamic processes (i.e., waves, tidal currents, and fluvial currents) involving sediment dynamic processes (i.e., traction, saltation, and suspension) [1,2]. Sediment dynamic processes provide the time-dependent coupling mechanism through which this adjustment takes place [1]. Hydrodynamic processes drive sediment dynamic processes resulting in morphodynamic change over time. Progressive modification of geomorphology, in turn, alters boundary conditions for the hydrodynamic processes, which evolve to produce further changes in sediment dynamic processes. Coastal evolution is the product of morphodynamic processes [1,2] that occur at different spatiotemporal scales [3–5] in response to changes in allogenic and autogenic processes [6–8]. The essential properties of coastal evolution are attributable to the feedback loop between morphodynamics and the hydrodynamics that drives sediment dynamics producing morphodynamic change [1]. Because of the complications of resuspension, settling and deposition, and particle flocculation, coastal sediment dynamics are particularly difficult to characterize [9–16].

Coastal sediment dynamics are well explored in a modern horizontal 2-D context in both estuaries [13,14,17–20] and back-barrier lagoons [21–26]. For example, Franz, Pinto, Ascione, Mateus, Fernandes, Leitão, and Neves [20] investigated the influence of the hydrodynamics (tidal currents and wind waves) on the cohesive sediment dynamics in the Tagus estuary, Portugal using the MOHID water modeling system [27]. Molinaroli, Guerzoni, De Falco, Sarretta, Cucco, Como, Simeone, Perilli, and Magni [25] revealed a general correlation between root mean square velocity (RMSV) and sortable silt in the lagoon of Cabras, and between RMSV and coarser sediments in the lagoon of Venice. However, coastal sediment dynamics are still very poorly constrained for ancient time-series studies.

Depositional processes are controlled partly by the hydraulic properties of the currents in question and partly by the size and density of the particles themselves [28,29]. Grain-size analysis is a basic tool for the process-based interpretation of grain-size distributions in which traction, saltation, and suspension populations are reflected in some manner [30–34]. It has been recognized that most frequency (or cumulative frequency) distribution curves of grain-size distributions are composed of two or more overlapping log-normally distributed grain-size populations [35,36]. Each grain-size population has been attributed to a different mode of sediment transport and deposition [17,35–39]. The decomposition of grain-size distributions into the fundamental populations provides proxy data for depositional process interpretation [32,36,37,40,41].

The Ximing Sandstone-to-No. 9 Coal succession of the Taiyuan Formation in the Linxing gas field was interpreted to record the complex internal architecture of a transgressive succession developed in the western coast of the late Pennsylvanian North China cratonic epeiric sea [42], making it an excellent case study for deciphering the coastal depositional responses to the relative sea-level rise in cratonic or epicontinental basins. This study performed facies, sequence stratigraphic, and grain-size analyses of the Ximing Sandstone-to-No. 9 Coal succession. The integrated facies, sequence stratigraphic, and grain-size analyses provide the language and concepts that allow complex coastal depositional process variability through the net-transgressive succession to be described, differentiated, and quantified.

2. Geological Setting

The assembly of the supercontinent Pangea from the Pennsylvanian to the Late Permian drove the west-to-east scissor-like closure of the Paleo-Asian Ocean [43] (Figure 1a) and triggered a basement uplift known as the Inner Mongolia Paleouplift (IMPU) along the northern margin of the North China Craton (NCC) [44] (Figure 1b). The Linxing gas field was located in an intermediate regional accommodation setting between the northern and southern edges of the western NCC (Figure 1b). The long-term sea level displays a gradual rise during the Pennsylvanian, attaining a peak in the early Permian (Asselian), followed by a gradual fall for the remainder of the Permian [45]. The long-term climate varied from tropical rainforest during the Pennsylvanian to Early Permian through Savanna in the early Middle Permian to subtropical arid during the late Middle to Late Permian [46]. The Permo-Pennsylvanian North China Basin lying inboard of the IMPU was a huge cratonic basin [44,47] in which sediments deposited were derived mainly from the rising IMPU to the north, the Qingyang Paleouplift to the west, and the Qinling Paleouplift to the south [48,49] (Figure 1b). The interaction of the basin subsidence, sea-level changes, climate, source-area uplift, and autogenic processes led to the deposition of coastal and epeiric shelf quartzose sandstones, grayish-black mudstones, limestones, and coal seams (i.e., Benxi and Taiyuan formations), fluvio-deltaic sandstones, grayish-black mudstones, and coal seams (i.e., Shanxi Formation), and inland fluvio-lacustrine yellowish-green sandstones and mudstones (i.e., Xiashihezi Formation) in 23 stratigraphic sequences (S1–S23). Accordingly, the tectonic evolution of the Permo-Pennsylvanian North China Basin was differentiated by Wu and Zhang [50] and Wu et al. [51] into the differential subsidence, uniform overlap, offlap, subsidence inversion, and intensive uplift/subsidence stages (Figure 1c). The Pennsylvanian–Permian boundary marking the onset of the subsidence inversion was

placed by Wang and Kang [52] at the lower contact of the Miaogou Limestone in the Xishan section of Taiyuan, across which the basin morphology changed from the north-dipping to the south-dipping, and the transgressive direction correspondingly changed from the northeast to the southeast (Figure 1b,c). The Ximing Sandstone-to-No. 9 Coal succession of sequence eight deposited during the late offlap stage can be correlated northward to the Palougou Limestone in the Palougou section (Figure 1c). Based on the constraint of the conodont-bearing limestone marker beds, the previously dated bentonitic tuff bed (298.925 ± 0.073 Ma) in the Palougou section [53] and Ximing Sandstone (302 ± 3 Ma) in the Liuchanggou section of Taiyuan [54], the Ximing Sandstone-to-No. 9 Coal succession in the study area is interpreted to be late Pennsylvanian (Gzhelien) in age (Figure 1c).

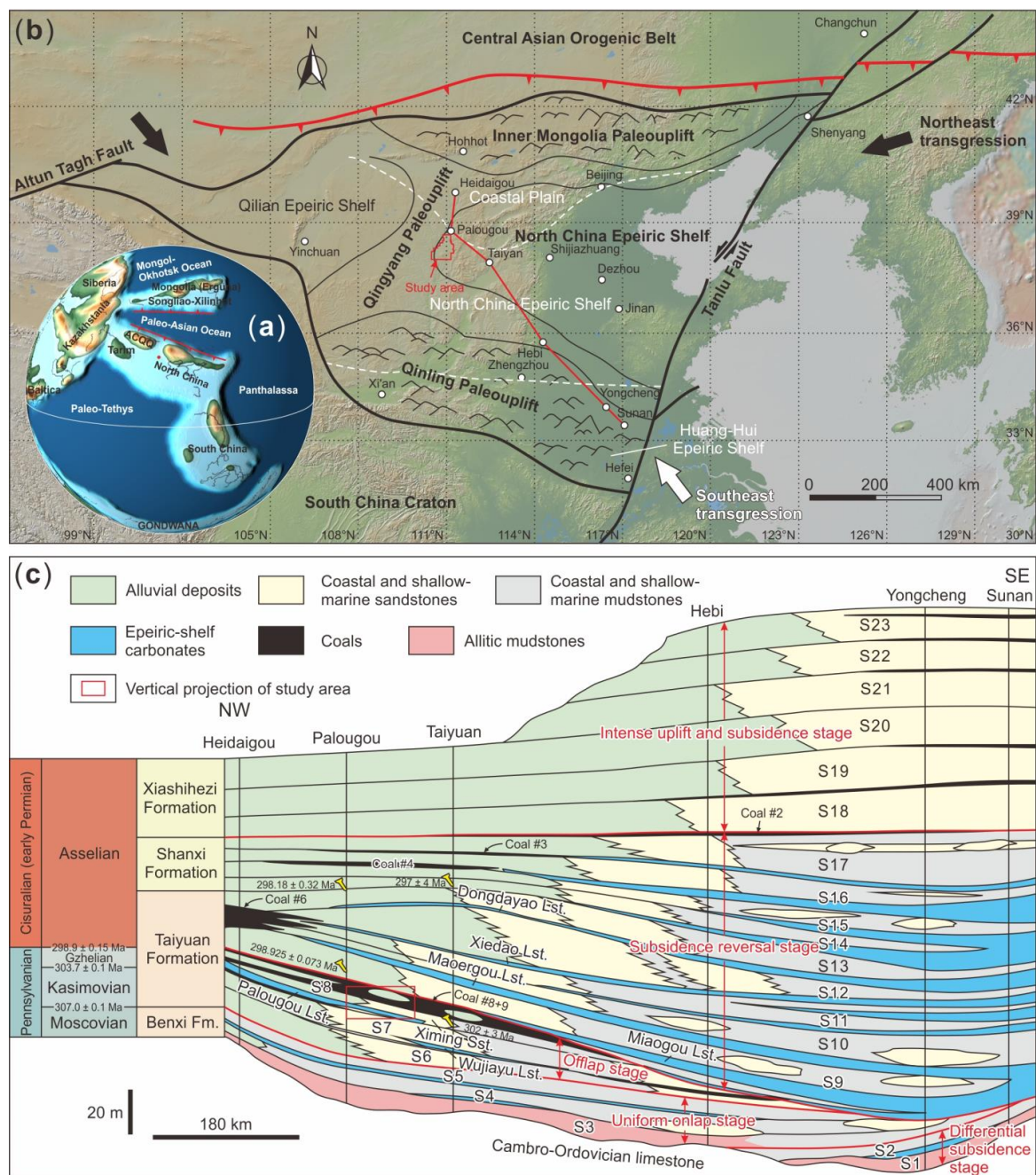


Figure 1. (a) The late Pennsylvanian (ca. 300 Ma) global paleogeographic map showing the location of the North China Block and the study area (red dot), obtained from <http://dinosaurpictures.org/ancient-earth#300>, accessed on 2 February 2022. Abbreviation: ACQQ—Alex, Central Qilian and

Qaidam. (b) Schematic, late Pennsylvanian (black fine lines and label; modified after Liu [55]) and early Permian (white dashed lines and label; modified after Jin and Shang [56]) paleogeographic maps of the North China Basin. Note the different transgressive directions during the two periods (black and white arrows, respectively, for late Pennsylvanian and early Permian). (c) Schematic, northwest–southeast cross-section across the North China Basin showing the sequence stratigraphic subdivisions of the Permo-Pennsylvanian Benxi, Taiyuan, Shanxi, and Xiashihezi formations comprising 23 sequences (modified from Wu and Zhang [50]). Age data are from Wu, Ramezani, Zhang, Wang, Zeng, Zhang, Liu, Chen, Cai, Hou, Liu, Yang, Henderson, and Shen [53] in the Palougou section and Sun, Zeng, Liu, Cui, and Wang [54] in the Liuchanggou section of Taiyuan. See (b) for track of the cross-section. The red box indicates the vertical projection of the study area to the cross-section.

3. Materials and Methods

Core and well-log data presented in this paper mainly involve the coal measure gas (i.e., coalbed methane, tight-sandstone gas, and shale gas) co-production demonstration project conducted by China United Coalbed Methane Corporation Limited across the Linxing gas field (Figure 2). Conventional cored wells TB-01, 02, 03, and LX-8 and 118 wireline-logged wells through the Ximing Sandstone-to-No. 9 Coal succession were collected (Figure 2). Cylinder cores in wells TB-01, 02, and 03 were slabbed by Bohai Oil Research Institute into 1/3 and 2/3 cores. After that, the cutting surfaces of the 1/3 cores were examined and logged at the centimeter to decimeter scale for a definition of lithofacies, facies associations, and bounding surfaces, whereas the 2/3 cores were reserved for further sampling. Gamma-ray and density well-log curves were used to extrapolate the sedimentological and sequence stratigraphic interpretations from the cored wells into the uncored wells. Discrete and random sampling was used, and the sampling frequency was determined based on observed lithofacies variability. In total, 68 samples were collected in cores TB-01, 02, 03, and LX-8 for grain-size measurements. The collected samples were digested with 10% H₂O₂ to remove organic matter and then with 10% HCl to dissolve carbonates. After that, the digested samples were repeatedly washed with deionized water and then disaggregated using 0.05 M (NaPO₃)₆ on an ultrasonic vibrator for 10 min. At last, grain-size determinations were carried out with a laser diffraction particle size analyzer (LMS-24). Textural nomenclature of siliciclastic rocks is based on the grain-size classification of Lazar et al. [57].

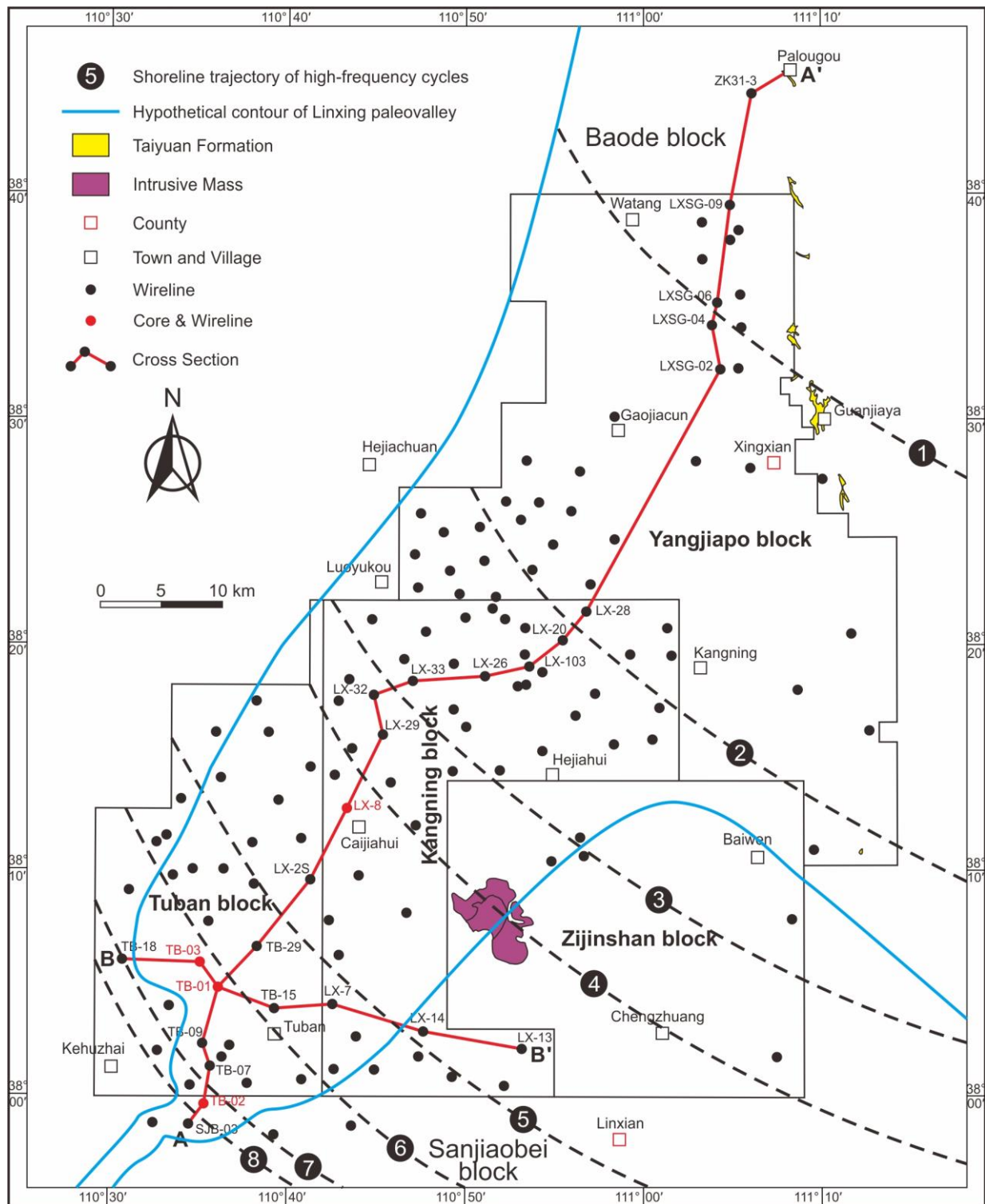


Figure 2. Simplified geological map of the study area illustrating locations of cores TB-01, 02, 03, and LX-8, wireline-logged wells, and tracks of cross-sections A–A’ and B–B’. The numbers represent the evolution of the paleoshoreline during the deposition of the Ximing Sandstone-to-No. 8 Coal succession, with ‘1’ representing the paleoshoreline just before the deposition of high-frequency cycle 2, ‘2’ to ‘7’ representing the maximum flooding paleoshoreline of each high-frequency cycle, and ‘8’ representing the turnaround from the transgressive to regressive shoreline trajectory. See Figure S1a,b for high-frequency cycles 1 to 8.

4. Results and Discussion

4.1. Facies Associations and Depositional Environments

Based on facies analysis of core and well-log data, 43 distinct lithofacies types and related depositional processes have been identified within the Ximing Sandstone-to-No. 9 Coal succession (Table 1). Grouping of genetically related lithofacies allowed the recognition of eight facies associations (Table 2). These facies associations organized in the sequence stratigraphic framework are illustrated in Figure S1a,b.

Table 1. Summary of lithofacies and related depositional processes of the Ximing Sandstone-to-No. 9 Coal succession.

Code	Lithofacies	Sedimentary Structures	Process Interpretation
Gcm	Granule- to pebble-sized, clast-supported conglomerate	Massive	Hyperconcentrated flow
Sm, mSm	Sandstone, muddy sandstone	Massive or faint lamination, locally spaced lamination, parallel oriented coal and/or carbonaceous mud clasts	Turbidity flow or hyperconcentrated flow
Sx, mSx, Sxd	Sandstone, muddy sandstone	Unidirectional crossbedding with or without mud drapes	Migration of 2D or 3D dunes under unidirectional currents. Drapes indicate periods of reduced energy in the system, possibly due to tidal fluctuations
Sbx, mSbx, Sbd	Sandstone, muddy sandstone	Bidirectional crossbedding with or without mud drapes	Migration of 2D or 3D dunes under bidirectional currents. Drapes indicate periods of reduced energy in the system, possibly due to tidal fluctuations
mSs	Muddy sandstone	Sigmoidal crossbedding	Lateral juxtaposition of laminated sandy units with sigmoidal geometry
Sp, mSp, sMp	Sandstone, muddy sandstone, sandy mudstone	Parallel lamination	Plane-bed flow (upper flow regime)
Sl	Sandstone	Low-angle lamination	Migration of straight or high wavelength bedforms in a transitional upper flow regime
mSl	Muddy sandstone	Fine lamination, small ripples	Overbank, abandoned channel, or waning flood deposits
Sr, Srd, mSrd, sMr	Sandstone, muddy sandstone, sandy mudstone	Current-ripple or climbing-ripple cross-lamination with or without mud drapes	Ripples (lower flow regime). Drapes indicate periods of reduced energy in the system, possibly due to tidal fluctuations
mSrn, mSin	Muddy sandstone	Rhythmic or irregular stacking of normally graded beds	Waning tidal currents with high suspended-sediment concentrations. Rhythmic stacking indicates spring–neap tidal cycles
Hrc	Sand-dominated heterolith	Rhythmic climbing-ripple cross-lamination	Unidirectional migration of ripples by lower flow regime currents under sustained high suspended-sediment concentration. The climbing ripples indicate rapid deposition from decelerating flows
Hrl	Sand-dominated or silt-dominated heterolith	Rhythmic lamination, locally strong bioturbation, or root casts	Bedload transport by tidal currents and waves alternating with suspension deposition by gravitational settling from slack water
Hh	Mixed sand (or coarse silt)–mud heterolith	Horizontal lamination	Bedload transport by upper flow regime currents alternating with suspension deposition during slack water conditions

Table 1. Cont.

Code	Lithofacies	Sedimentary Structures	Process Interpretation
Hi	Mixed sandstone–mudstone heterolith	Cm-scale interbedding	Bedload transport by steady flows alternating with suspension deposition by dynamic settling
sMhx	Sandy mudstone	Hummocky cross-lamination	High-intensity, storm-wave-produced oscillatory flows or oscillatory-dominated combined flows with high aggradation rates
sMpl	Sandy mudstone	Planar-parallel to low-angle cross-lamination with stacked, normal, and inverse grading	Sustained lateral sediment transport by waning and/or waxing tidal currents, waves, or turbulent currents
sMc	Sandy mudstone	Convolute lamination	Entrapped air
sMm	Sandy mudstone	Homogeneous or faint lamination locally with mud clast	High-intensity oscillatory-dominated combined flows with high depositional rates suppressing grain traction. Significant reworking of the substrate with production of coarse-grained detritus
sMri	Sandy mudstone	Rhythmic stacking of inversely graded beds with fine lamination	Waxing tidal currents with high suspended-sediment concentrations
sMwr, sMcf, sMI	Sandy mudstone	Wave-ripple cross-lamination, combined-flow-ripple cross-lamination, low-angle lamination	Storm-wave-produced oscillatory flows or oscillatory-dominated combined-flows
mMh	Medium mudstone	Homogeneous and unbioturbated	Fluid mud deposits
mMI	Medium mudstone	Fine lamination	Gravitational particle-by-particle fallout and migrating floccule ripples
mMm	Medium mudstone	Massive to faint lamination, sparse to moderate bioturbation	Gravitational particle-by-particle fallout and migrating floccule ripples. Primary sedimentary structures destroyed by bioturbation
sMs	Sandy mudstone	Silt or sand streaks	Gravitational particle-by-particle fallout frequently interrupted by sand, silt, and fluid mud deposition from low-intensity, storm-wave-produced oscillatory flows, and oscillatory-dominated combined-flows
cbMI, cbMm,	Carbonaceous mudstone	Fine lamination, massive or faint lamination,	Limnotrophic pond
mC	Muddy coal	Mud (30 to 60%) either in intimate mixture with coal or in separate thin (<5 mm) bands	Limnotrophic mire
bC	Bright coal	Dominantly bright coal containing thin (<5 mm) dull coal bands (<10%)	Ombrotrophic mire
baC	Banded coal	Contains bright and dull coal bands (<5 mm; 40% to 60%)	Transitional rheotrophic mire
dC	Dull coal	Dominantly dull coal containing thin (<5 mm) bright coal bands (<10%)	Rheotrophic mire

Table 2. Summary of facies associations and related depositional (sub)environments of the Ximing Sandstone-to-No. 9 Coal succession.

Depositional Environments (FA)	Depositional Subenvironments	Constituent Lithofacies
Fluvial channel (FA1)	Channel fill Channel fill or lower point bar	mSm mSx
Tidal–fluvial channel (FA2)	Channel fill Channel fill or lower intertidal point bar Lower to middle intertidal point bar Middle intertidal point bar Upper intertidal point bar	Gcm, Sm, mSm, mMh Sx, mSx, Sbx, mSbx, Sxd, Sbd, mSs Srd, Sxd, Sbd, Sp, Sl Hrl, Hi Hrc
Upper flow regime sand flat (FA4)	None	mSp, mMh
Estuarine tidal bar (FA3)	Estuary-head tidal bar (bayhead delta) Tidal dune (compound dune) Elongate tidal bar	mSx mSx mSx, mSrd
Fringing tidal flat (FA5)	Sand flat Mixed flat Mud flat Salt marsh	mSrd, mSxd, mSin mSrn sMl, sMm, sMri Hrl
Lagoonal tidal shoreface (FA6)	Lagoonal mud flat Lagoonal beach Lagoonal upper shoreface and/or beachface Lagoonal lower shoreface	Hrl, mMl mSm, mSp sMwr, sMp mMl, sMs, sMwr, sMhx, mMm, sMm, sMp, sMr
Back-barrier lagoon (FA7)	Lagoonal fines Washover fan Flood-tidal delta Secondary tidal channel Washover channel Back-barrier tidal flat	mMl, mMm sMp sMs, sMp, sMr sMp, sMr sMm, sMc Hh
Lagoonal coastal mire (FA8)	None	cbMl, mC, bC, baC, dC

4.1.1. Facies Association 1 (FA1): Fluvial Channel

Description: FA1 mainly occurs in the Ximing Sandstone in the northwestern Sanjiaobei and southern Tuban blocks (Figure S1a). The lithofacies of FA1 stack vertically into an erosively based, blocky to fining-upward succession (Figure S1a). This succession is up to 4.71 m thick (2130.18–2125.47 m) in core TB-02 and consists dominantly of massive muddy sandstone (mSm) topped by unidirectional cross-bedded muddy sandstone (mSx; Figure 3). Lithofacies mSm commonly exhibit faint lamination, with sparsely spaced planar lamination.

Interpretation: FA1 is interpreted to represent the deposition of fluvial channels within the inner extension of a tight meander bend in the inner estuary [58]. Lithofacies mSm with faint and/or spaced planar lamination indicates deposition of within-channel turbidites originated by breach failures in the channel margin [59]. Lithofacies mSx is interpreted to have been formed in the channel thalweg and/or on the lower point bar [60,61].

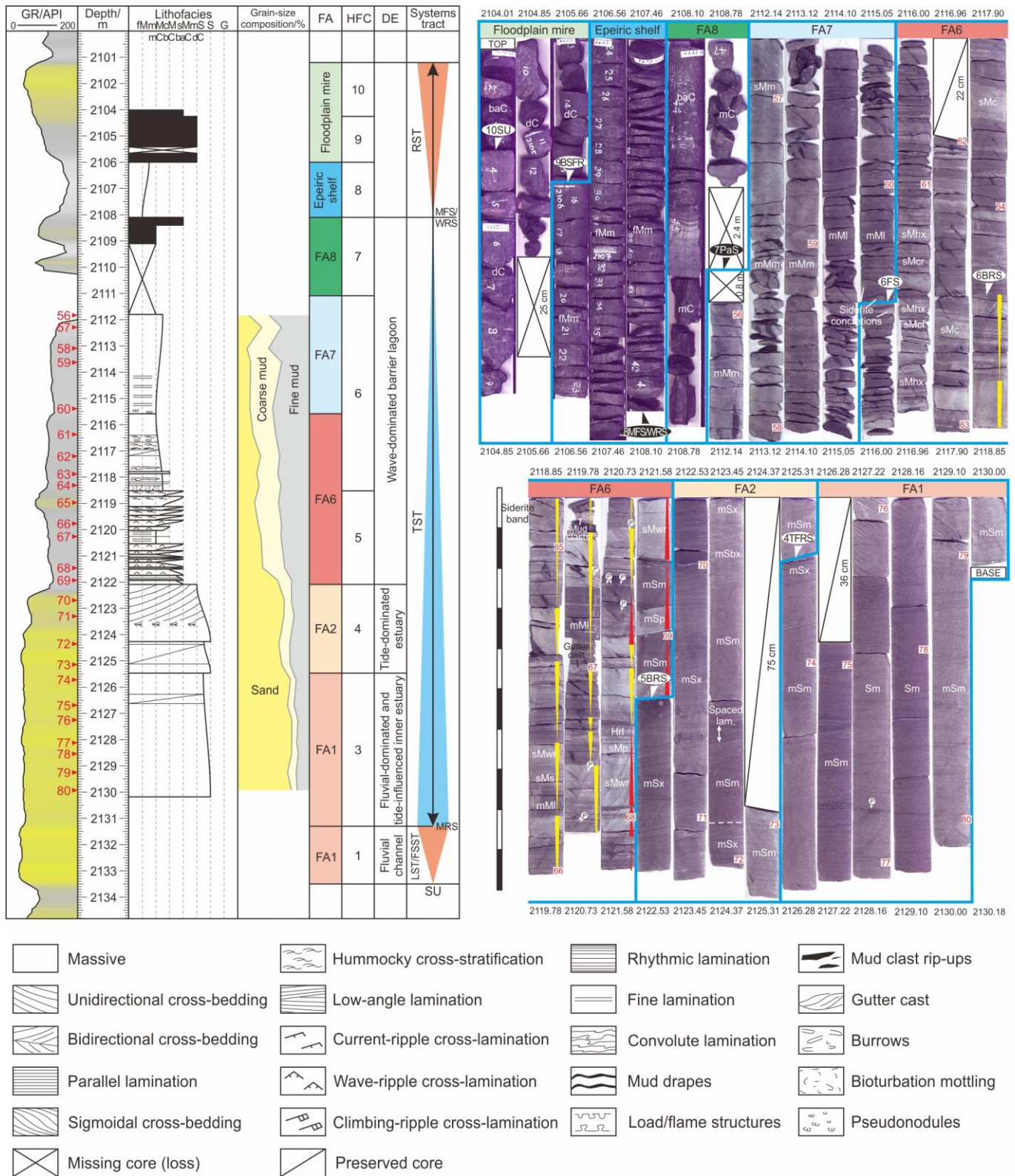


Figure 3. Panoramic view and graphic log of core TB-02 through the Ximing Sandstone-to-No. 8 Coal succession showing lithofacies, facies associations (FA), depositional environments (DE), high-frequency cycles (HFC), systems tracts, stratigraphic surfaces, and sampling positions. See Figure S1a for the cored interval of well TB-02. Refer to the legend in Figure S1 for definition of acronyms, colors, and symbols used in this figure. Abbreviations: FSST—falling-stage systems tract; LST—lowstand systems tract; TST—transgressive systems tract; RST—regressive systems tract.

4.1.2. Facies Association 2 (FA2): Tidal–Fluvial Channel

Description: FA1 passes northeastward by following the Ximing Sandstone into FA2 in the northwestern Sanjiaobei and southern Tuban blocks (Figure S1a). The lithofacies of FA2 stack vertically to form an erosively based, blocky to fining-upward succession that ranges in thickness from 2 to 5 m (Figure S1a,b). The stacked blocky succession of four FA2 is up to 13.62 m thick (2087.12–2073.50 m) in core TB-03 (Figure 4). The lowermost FA2 is 4.05 m thick (2087.12–2083.07 m) and grades upward from massive (Sm) and unidirectional cross-bedded sandstone (Sx) to mud-draped, ripple cross-laminated sandstone (Srd; Figure 4). Mud-draped unidirectional cross-bedded (Sxd), bidirectional cross-bedded (Sbd), parallel (Sp), and low-angle laminated sandstone (Sl) are found intercalated within the Srd (Figure 4). The succeeding FA2 is 4.37 m thick (2083.07–2078.70 m) and transitions upward from Sm through Sx to Sxd (Figure 4). Granule- to pebble-sized, clast-supported massive conglomerate (Gcm) beds (7 to 20 cm thick) are found intercalated within the Sxd (Figure 4). The third FA2 is 4.96 m thick (2078.70–2073.74 m) and transitions upward from homogeneous and unbioturbated medium mudstone (mMh) through mud-draped (or not), unidirectional cross-bedded sandstone (Sx, Sxd) to massive muddy sandstone (mSm; Figure 4). Lithofacies Srd is found locally intercalated within the Sx (Figure 4). The cored 24 cm (2073.74–2073.50 m) of the uppermost FA2 is composed of bidirectional cross-bedded sandstone (Sbx; Figure 4).

Three separate FA2 are recognized in core TB-01 (Figure 5). The lowermost FA2 is 3.18 m thick (1973.53–1970.35 m) and consists of a massive muddy sandstone (mSm) bed (24 cm thick) erosively overlain by mud-draped, unidirectional cross-bedded muddy sandstone (mSxd; Figure 5). Lithofacies mSxd grades upward into sigmoidal cross-bedded sandstone (mSs) followed by rhythmically laminated heterolith (Hrl; Figure 5). Centimeter-scale interbedded sandstone and mudstone heterolithic bed (Hi; 6 cm thick) is found intercalated within the Hrl (Figure 5). Crossbedding appears to change its inclination to the opposite direction through sandstone successions of the meter scale. The cored 27 cm (1966.20–1965.93 m) of the succeeding FA2 consists predominantly of massive muddy sandstone (mSm) exhibiting spaced planar and/or faint lamination with parallel-oriented coal or carbonaceous mud clasts (Figure 5). The uppermost FA2 is 46 cm thick (1956.78–1956.32 m) and consists of rhythmically climbing-ripple cross-laminated heterolith (Hrc) with basal homogeneous and unbioturbated medium mudstone bed (mMh; Figure 5).

FA2 is up to 3.38 m thick (2125.47–2122.09 m) in core TB-02, in erosional contact with the underlying FA1, and consists of massive muddy sandstone (mSm) overlain by and interstratified with unidirectional or bidirectional cross-bedded muddy sandstone (mSx, mSbx; Figure 3). Lithofacies mSm exhibits some spaced planar and/or faint lamination.

Interpretation: FA2 is interpreted to represent the deposition of tidal–fluvial channels within a tight meander in the inner estuary [58]. Lithofacies Sm or mSm with spaced planar and/or faint lamination are interpreted as within-channel turbidite sequences generated by breach failures in the channel margin [59]. Lithofacies Sx, mSx, Sxd, Sbx, mSbx, Sbd, and mSs are all interpreted to have been formed in the channel thalweg and/or on the lower intertidal point bar [14,60,62,63]. The basal and/or intervening mMh layers are interpreted as channel-bottom fluid mud deposits [64]. The intervening Gcm layers are interpreted to represent hyperconcentrated flow deposits in the channel [65]. The predominance of Srd with intervening Sxd, Sbd, Sp, and Sl beds is interpreted to indicate deposition of lower to middle intertidal point bars [66]. Lithofacies Hrl is interpreted to have been formed on the middle intertidal point bar over semidiurnal to neap–spring tidal cycles [67,68], in which the intervening Hi bed indicates deposition with high suspended-sediment concentrations over semidiurnal tidal cycles [69]. Lithofacies Hrc is interpreted to have been formed on the upper intertidal point bar [70]. The inversion of bedding inclination through cross-bedded successions of meter scale or between the different lithofacies suggests a conversion of the paleocurrent direction (e.g., from flood- to ebb-dominated) [71].

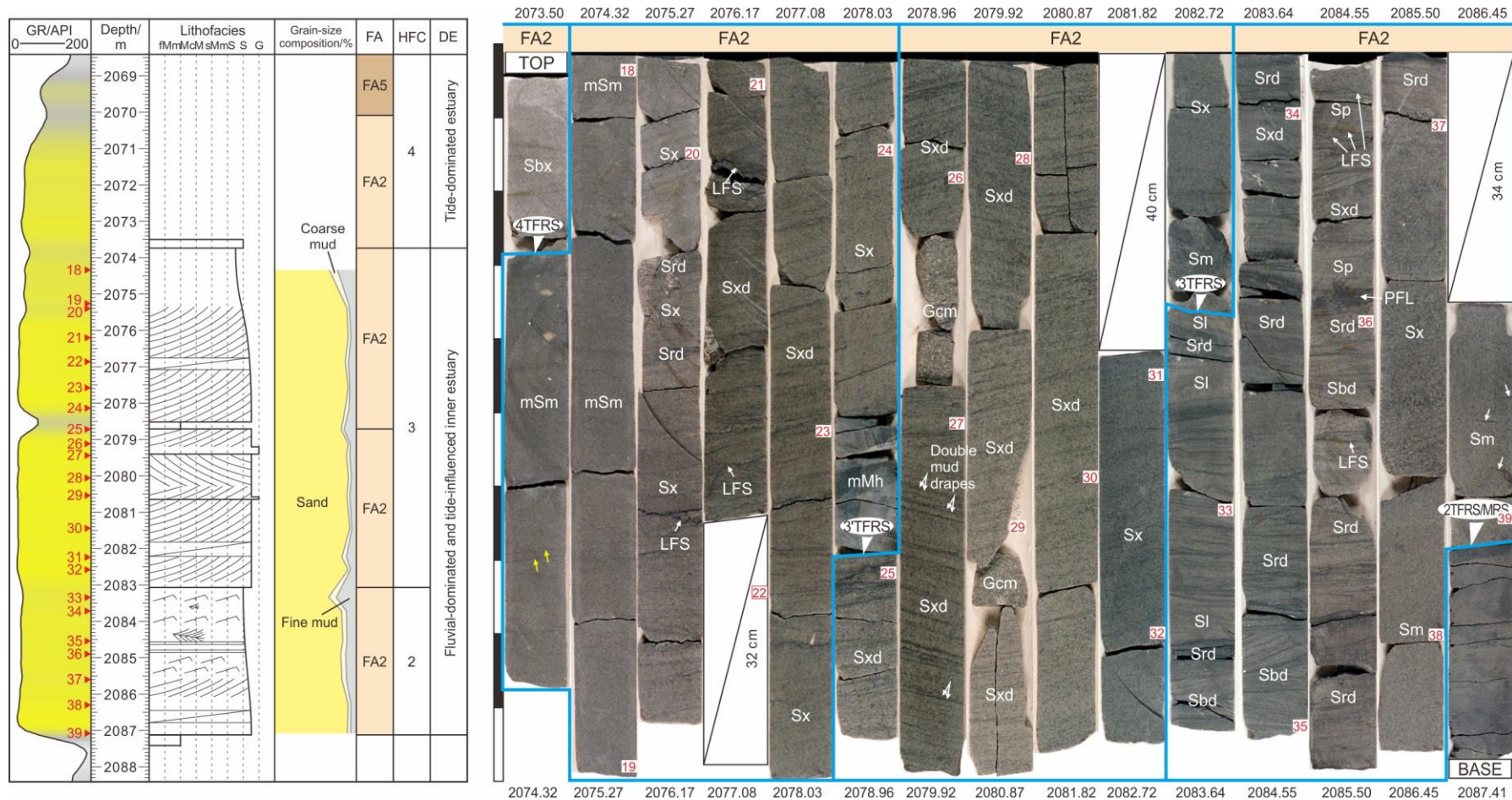


Figure 4. Panoramic view and graphic log of core TB-03 through the Ximing Sandstone showing lithofacies, facies associations (FA), depositional environments (DE), high-frequency cycles (HFC), stratigraphic surfaces, and sampling positions. See Figure S1b for the cored interval of well TB-03. Refer to the legend in Figures S1 and 3 for definition of acronyms, colors, and symbols used in this figure. Abbreviations: LFS—load/frame structures; PFL—plant fragment-rich layer.

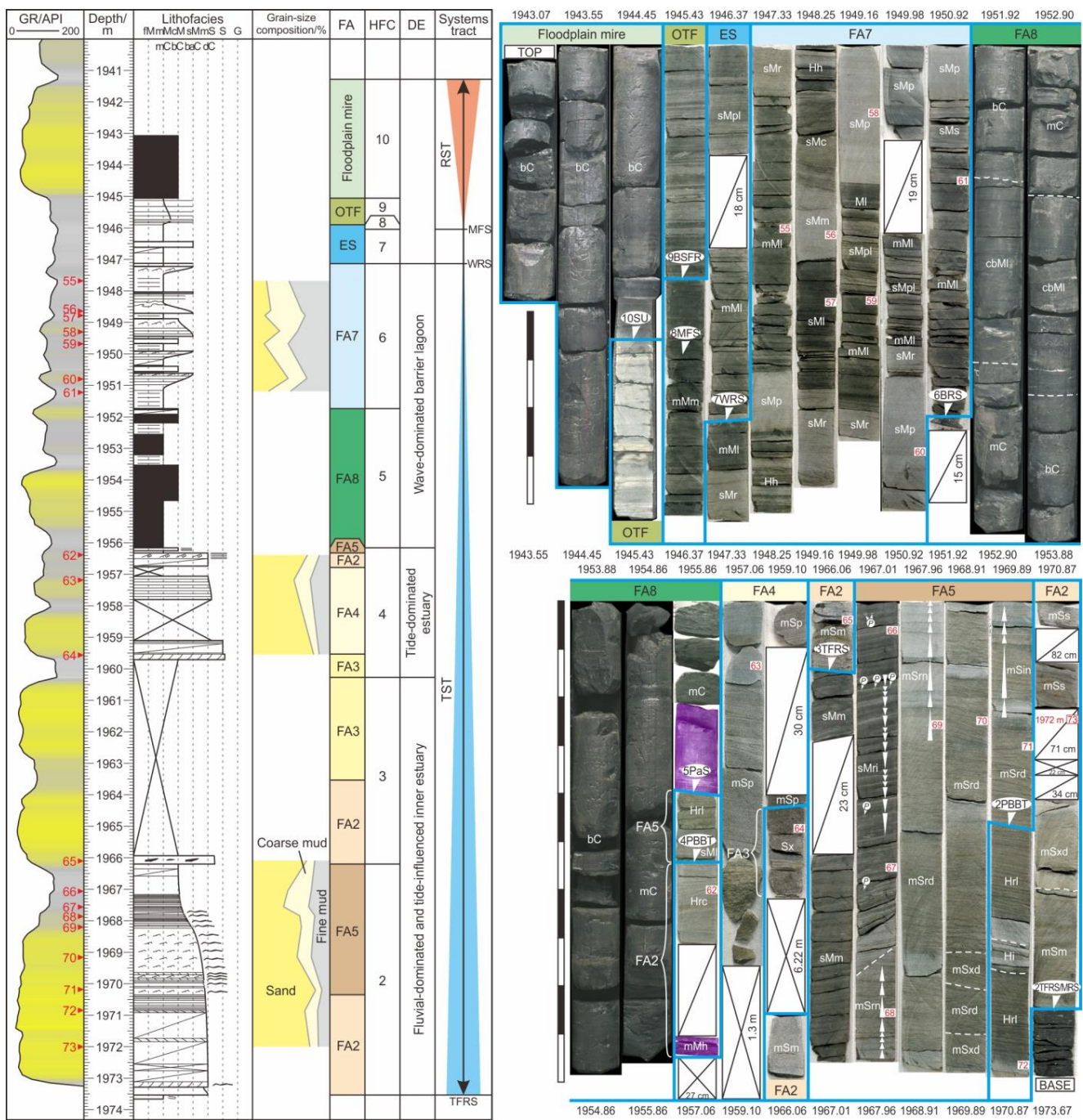


Figure 5. Panoramic view and graphic log of core TB-01 through the Ximing Sandstone-to-No. 8 Coal succession showing lithofacies, facies associations (FA), depositional environments (DE), high-frequency cycles (HFC), systems tracts, stratigraphic surfaces, and sampling positions. See Figure S1a,b for the cored interval of well TB-01. Refer to the legend in Figures S1 and 3 for definition of acronyms, colors, and symbols used in this figure. Abbreviations: ES—epeiric shelf; OTF—open-coast tidal flat; TST—transgressive systems tract; RST—regressive systems tract.

4.1.3. Facies Association 3 (FA3): Estuarine Tidal Bar

Description: FA2 passes northeastward by following the Ximing Sandstone into FA3 in the northern Tuban and western Kangning blocks (Figure S1a). The lithofacies of FA3 stack vertically to form an erosively based, coarsening- or fining-upward succession that ranges in thickness from 2.7 to 6.3 m (Figure S1a,b). FA3 consists dominantly of unidirectional cross-

bedded muddy sandstone (mSx) with subordinate mud-draped, ripple cross-laminated muddy sandstone (mSrd; Figure 6a,c). Centimeter-scale mud interlayers and single and double mud drapes are commonly present in this facies association (Figure 6a,b). The bipolar cross-stratification is locally observed in the meter-scale sandstone succession.

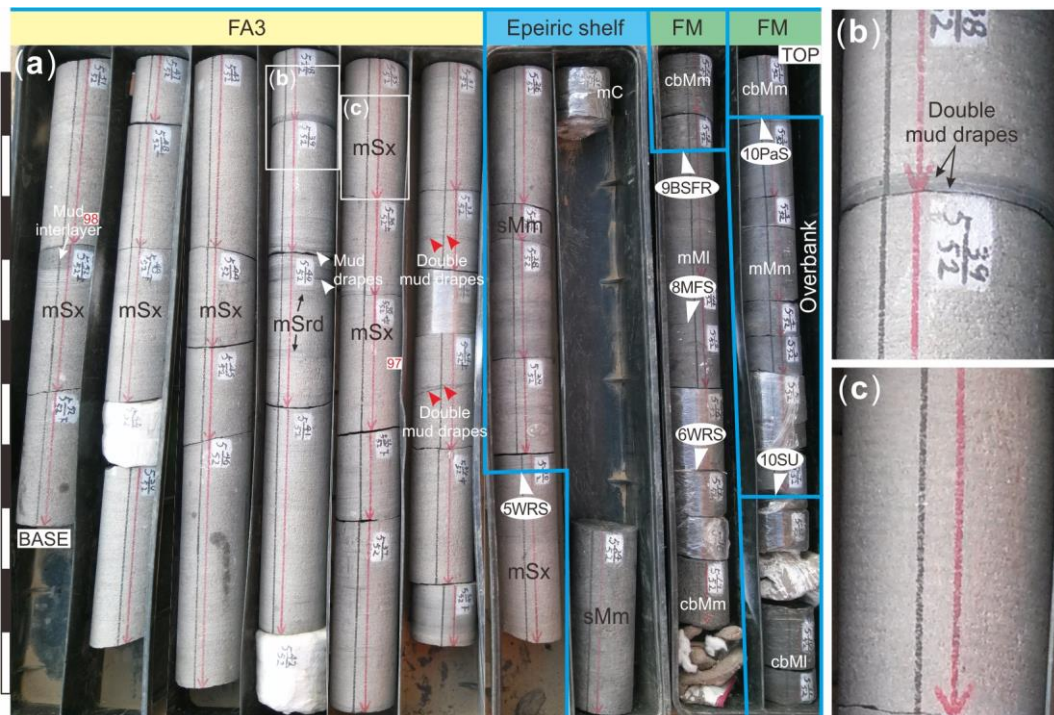


Figure 6. (a) Panoramic view of core LX-8 through the Ximing Sandstone-to-No. 8 Coal succession showing lithofacies, facies associations (FA), stratigraphic surfaces, and sampling positions; (b) Close-up view of double mud drapes shown in (a); (c) Close-up view of unidirectional crossbedding shown in (a). See Figure S1a for the cored interval of well LX-8. Refer to the legend in Figure S1 for definition of acronyms, colors, and symbols used in this figure. Abbreviation: FM—floodplain mire.

Interpretation: FA3 is interpreted to represent the deposition of estuarine tidal bars [58,72]. Lithofacies mSx arranged in the coarsening-upward succession is interpreted to have resulted from the progradation of estuary-head tidal bars (i.e., bayhead deltas) into the estuary central basin [73–75] or from forward accretion of tidal dunes (i.e., compound dunes [71,76,77]). Lithofacies mSx arranged in the fining-upward succession is interpreted to have resulted from lateral accretion of elongate tidal bars [19,71,77]. Here, we prefer the term “estuarine tidal bar” for any positive architectural units composed of stacked dunes within the funnel basin of an estuary. The tidal influences are indicated by the presence of single and double mud drapes and bipolar cross-stratification. The bipolar cross-stratification indicates mutually evasive channels used by flood and ebb currents [19,58].

4.1.4. Facies Association 4 (FA4): Upper Flow Regime Sand Flat

Description: FA4 occurs between FA2 and FA3 in high-frequency cycle four in the middle Tuban block (Figure S1a). The lithofacies of FA4 stack vertically to form an overall fining-upward succession. This succession is up to 2.75 m thick (1959.53–1956.78 m) in core TB01, in sharp and conformable contact with the underlying FA3 (Figure 5). FA4 consists predominantly of fine-grained, parallel laminated muddy sandstone (mSp) with an intervening homogeneous and unbioturbated medium mudstone (mMh) layer 40 cm thick (1958.5–1958.1 m; Figure 5). Parallel lamination is observed to be gently dipping throughout the succession and change its inclination to the opposite direction through meter-scale successions.

Interpretation: FA4 is interpreted to represent the deposition of upper flow regime (UFR) sand flats [14]. The gently dipping parallel lamination is interpreted to have been developed on the lee and lateral sides of the faintly braided tidal bars in shallow estuaries [14]. The opposite inclination through the meter-scale mSp succession represents a conversion of the paleocurrent direction (e.g., from flood- to ebb-oriented). The intervening mMh layer represents fluid mud deposition by the interaction of saline and fresh waters in the turbidity-maximum zone [64]. The development of UFR sand flats typically indicates a macrotidal estuarine environment [14].

4.1.5. Facies Association 5 (FA5): Fringing Tidal Flat

Description: FA5 mainly occurs in the Ximing Sandstone in the Tuban and southern Kangning blocks (Figure S1a,b). The lithofacies of FA5 stack vertically into a distinct fining-upward succession in sharp and conformable contact with the underlying FA2. Two separate FA5 are recognized in core TB-01 (Figure 5). The lower FA5 is 4.15 m thick (1970.35–1966.20 m) and transitions upward from mud-draped ripple cross-laminated muddy sandstone (mSrd) through rhythmically stacked, normally graded muddy sandstone (mSrn) and inversely graded sandy mudstone (sMri) bedsets (each bed 2–10 cm thick) to massive or faintly laminated sandy mudstone (sMm; Figure 5). Mud-draped, cross-bedded muddy sandstone (mSxd) beds (6–8 cm thick) and irregularly stacked, normally graded muddy sandstone (mSin) bedset (each bed 2–10 cm thick) are found intercalated within the mSrd (Figure 5). Individual mSin bed display, from base to top, an erosional base, parallel lamination, and climbing-ripple cross-lamination that may be overlain by a mud drape (Figure 5). Individual mSrn beds vary in thickness upward from a gradual decrease to a gradual increase and predominantly exhibit climbing-ripple cross-lamination that passively drapes or erosively overlies the preceding bed and may be overlain by a mud drape (Figure 5). Individual sMri beds are predominantly composed of finely laminated silt- or sand-streaked sandy mudstone (Figure 5). Overall, bioturbation ranges from absent in the muddy sandstone interval to sparse in the mudstone interval and consists dominantly of *Planolites*. The upper FA5 is 16 cm thick (1956.32–1956.16 m) and transitions upward from finely laminated mudstone (sMl) to rhythmically laminated heterolith (Hrl) of greenish-gray, rooted silt and dark mud (Figure 5).

Interpretation: FA5 is interpreted to represent the deposition of fringing tidal flats [14,71]. Lithofacies mSrd with intervening mSxd and mSin beds is interpreted to have been deposited on sand flats of the fringing tidal flat. Lithofacies mSrd passing upward into the mSrn represents a transition from the sand flats to mixed flats. Lithofacies sMri, sMm, and sMl are interpreted to have been formed on mud flats of the fringing tidal flat. Lithofacies Hrl is interpreted to have been deposited on salt marshes of the fringing tidal flat [78]. Individual normally (mSin, mSrn) and inversely graded (sMri) beds are interpreted to have been deposited by waning and waxing currents, respectively, with high suspended-sediment concentrations during the flood or ebb half of a tidal cycle [79–81]. The rhythmic stacking pattern of the mSrn and sMri beds indicates spring–neap tidal cycles, in which thicker and thinner graded beds represent deposition during spring and neap tides, respectively [71,79,82].

4.1.6. Facies Association 6 (FA6): Lagoonal Tidal Shoreface

Description: The lithofacies of FA6 stack vertically into an overall fining-upward succession overlying FA2 or overbank deposits in the northwestern Sanjiaobei block (Figure S1a). In core TB-02, FA6 is up to 6.42 m thick (2122.09–2115.67 m), transitions upward from stacked package (84 cm thick; 2122.09–2121.25 m) of six erosively based fining-upward units through stacked package (2.73 m thick; 2121.25–2118.52 m) of 14 coarsening-upward units (except one fining-upward unit) to an overall fining-upward mudstone interval (2.85 m thick; 2118.52–2115.67 m), and displays overall increasing-upward bioturbation from sparse (BI = 1) to moderate (BI = 2; Figure 3). The lowermost two fining-upward units range in thickness from 16 to 20 cm and are predominantly composed of massive

(mSm) and/or parallel laminated muddy sandstone (mSp; Figure 3). The overlying four fining-upward units range in thickness from 2 to 22 cm and consist dominantly of wave-ripple cross-laminated (sMwr) and/or parallel laminated sandy mudstone (sMp) followed by rhythmically laminated heterolith (Hrl) and/or finely laminated medium mudstone (mMl; Figure 3). The 16 individual coarsening-upward units range in thickness from 4 to 38 cm and consist dominantly of finely laminated medium mudstones (mMl) and/or silt- or sand-streaked sandy mudstones (sMs) followed by wave-ripple (sMwr) and/or hummocky cross-laminated sandy mudstone (sMhx; Figure 3). The overall fining-upward mudstone interval consists dominantly of homogeneous or faintly laminated medium mudstones (mMm) and silt- or sand-streaked sandy mudstones (sMs) interstratified with erosively based sandy mudstone beds (Figure 3). Individual sandy mudstone beds range in thickness from 1 to 12 cm and exhibit mud clast-bearing massive bedding (sMm), parallel lamination (sMp), hummocky cross-lamination (sMhx), wave-ripple (sMwr), current-ripple (sMr) or combined-flow-ripple cross-lamination (sMcf), convolute lamination (sMc) and/or gutter casts (Figure 3). Siderite bands and concretions occur sporadically throughout the mudstone-dominated interval (Figure 3).

Interpretation: FA6 is interpreted to represent the deposition of lagoonal tidal shorefaces. The “tidal shoreface” model of Dashtgard et al. [83] was used to combine tidal flats and beaches/shorefaces of the lagoonal shoreline. The overall fining-upward succession with component fining- and coarsening-upward units represents long-term lagoonal shoreline transgression punctuated by short-term progradation (i.e., shallowing-upward cycles) and flooding events. Lithofacies mSm and/or mSp in the individual fining-upward units reflect shallowing from distal to proximal beaches. The upward gradation from sMwr and/or sMp to Hrl and/or mMl in the individual fining-upward units represents shallowing from upper shorefaces and/or beachfaces to mud flats. The upward gradation from mMl and/or sMs to sMwr and/or sMhx in the individual coarsening-upward units reflects shallowing from distal to proximal lower shorefaces of the lagoon. The predominance of mMm and sMs in the overall fining-upward mudstone interval represents the deposition of distal lower shorefaces of the lagoon. The intervening sandy mudstone beds exhibiting sMm, sMp, sMhx, sMwr, sMr, sMcf, and/or gutter casts indicate deposition by storm-wave-produced oscillatory flows or oscillatory-dominated combined-flows [84,85].

4.1.7. Facies Association 7 (FA7): Back-Barrier Lagoon

Description: FA6 passes northeastward into FA7 in the northwestern Sanjiaobei and Tuban blocks (Figure S1a,b). In core TB-01, the lithofacies of FA7 stack vertically to form an overall fining-upward succession up to 4.61 m thick (1951.74–1947.13 m) that pinches out beneath epeiric shelf deposits at its down-dip termination (Figure S1a,b) and consists dominantly of finely laminated medium mudstone (mMl) with intervening sandy mudstone beds (Figure 5). The individual intervening sandy mudstone beds range from 12 to 57 cm thick and transitions upward from gradationally based, silt- or sand-streaked sandy mudstone (sMs) through parallel laminated sandy mudstone (sMp) to ripple cross-lamination (sMr) from erosively based sMp to sMr, or from erosively based massive sandy mudstone (sMm) through convolute-laminated sandy mudstone (sMc) to horizontally laminated heterolith (Hh) erosively overlain by an sMp bed (Figure 5). In core TB-02, the lithofacies of FA7 stack vertically into a coarsening-upward succession up to 3.87 m thick (2115.67–2111.80 m) that pinches out against FA6 at its up-dip termination (Figure S1a) and transitions upward from mMl to massive medium mudstone (mMm) or sandy mudstone (sMm; Figure 3). Both lithofacies mMl and mMm in cores TB-01 and 02 commonly contain different amounts of diagenetic dolomite (0–10%), pyrite (1–3%), and siderite (0–9%) concretions.

Interpretation: FA7 is interpreted to represent the deposition of back-barrier lagoons. Lithofacies mMl and mMm with diagenetic dolomite, pyrite, and siderite concretions are interpreted as lagoonal fines [86–88]. The intervening sandy mudstone beds exhibiting gradationally based sMs → sMp → sMr profile and erosively based sMp → sMr, sMm → sMc, or sMp profile are interpreted as flood-tidal deltas, secondary tidal channels, washover

channels, and washover fans, respectively [89–92]. Lithofacies sMc is interpreted to have resulted from pore fluid escape of the rapidly deposited and poorly packed washover channels [92]. Lithofacies Hh sandwiched between the underlying sMc and overlying sMp are interpreted as back-barrier tidal flats. The overall fining-upward trend of FA7 in core TB-01 represents the deepening of the seaward lagoon due to the barrier shoreline transgression, in which the intervening flood-tidal delta, secondary tidal channel, washover channel, and washover fan deposits represent barrier remnants. The coarsening-upward trend of FA7 in core TB-02 represents the gradual filling of the landward lagoon, where high sedimentation rates coupled with moderate base-level rise led to progradational trends despite the overall transgression of the barrier shoreline.

4.1.8. Facies Association 8 (FA8): Lagoonal Coastal Mire

Description: FA8 occurs as three individual coal seams (No. 9 Coal) associated with FA6 and FA7 at successively higher stratigraphic levels in the Sanjiaobei, Tuban, and southern Kangning blocks, with the upper more southwestward than the lower (Figure S1a). The lithofacies of FA8 stack vertically to form an overall shaling-upward coal succession overlying FA5, FA6, or FA7 and underlying FA7 or epeiric shelf deposits. FA8 is up to 4.42 m thick (1956.16–1951.74 m) in core TB-01 and composed of multiple stacked, fundamental brightening-upward units (1.85 to 2.67 m thick) of finely laminated carbonaceous mudstone (cbMl) and/or muddy coal (mC) to bright coal (bC), as indicated by individual decreasing-upward trends superimposed on the overall increasing-upward trend in gamma-ray and density signatures (Figure 5).

Interpretation: FA8 is interpreted to represent the deposition of lagoonal coastal mires. The overall shaling-upward coal succession with component brightening-upward units represents the onshore expression of the long-term lagoonal shoreline transgression punctuated by short-term shallowing-upward cycles and flooding events. The upward gradation from cbMl and/or mC to bC in each fundamental brightening-upward unit reflects shallowing from rheotrophic to ombrotrophic lagoonal coastal mire.

4.2. Stratigraphic Architecture and Depositional Evolution

Based on the observation of stratal stacking patterns of FA1 to FA8 recognized above, the Ximing Sandstone-to-No. 9 Coal succession of the Taiyuan Formation in the Linxing gas field can be subdivided into seven distinct high-frequency stratigraphic cycles (HFC-1 to 7) that can be correlated and mapped across the study area (Figure S1a,b). Each cycle ranges in thickness from 2.5 to 9 m and displays a fining- or coarsening-upward trend bounded by high-frequency tidal-, fluvial- and/or bay-ravinement surfaces, or a shaling-upward coal succession bounded below by paludification surface (Figure S1a,b). HFC-1 contains only relatively coarser-grained fluvial channel (FA1) deposits that are interpreted to have been formed during the falling- and/or lowstand stage [93,94]. The fluvial channel (FA1), tidal-fluvial channel (FA2), estuarine tidal bar (FA3), and fringing tidal flat deposits (FA5) in HFC-2 and 3 together define a fluvial-dominated and tide-influenced inner estuarine environment (Figure S1a,b). This inner estuary is inferred to be part of a mixed-energy barrier estuarine system cf. [58] based on the recognition of the estuary central basin and barrier complex deposits in the northern Kangning and Yangjiapo blocks, which pass northeastward into epeiric shelf deposits in the northern Yangjiapo and Baode blocks (Figure S1a). The fluvial channel (FA1), tidal-fluvial channel (FA2), estuarine tidal bar (FA3), UFR sand flat (FA4), and fringing tidal flat (FA5) deposits in HFC-4 (Figure S1a,b) together define a tide-dominated estuarine system cf. [14,58]. The lagoonal tidal shoreface (FA6), back-barrier lagoon (FA7), and lagoonal coastal mire (FA8) deposits in HFC-5, 6, and 7 together define a wave-dominated barrier lagoonal system cf. [95,96] (Figure S1a,b). The mixed-energy barrier estuary, tide-dominated estuary, wave-dominated barrier lagoon, and epeiric shelf deposits in HFC-2 to 7 are stacked vertically to form a transgressive systems tract (TST) that displays a backstepping shoreline trajectory (Figure 2) and an overall fining- and deepening-upward trend (Figure S1a,b). The transgressive estuarine

to lagoonal deposits are observed to have accumulated below a wave-ravinement surface (WRS) but above a maximum regressive surface (MRS) that seaward (i.e., northeastward) is successively reworked and replaced by a tidal/fluvial ravinement surface (TFRS), bay-ravinement surface (BRS), tidal-ravinement surface (TRS), and the WRS (Figure S1a). The transgressively modified MRS is observed to be separated from the subaerial unconformity (SU) by the falling-stage and/or lowstand fluvial channel (FA1) deposits in HFC-1 (Figure S1a). Lateral correlation of the Ximing Sandstone across the study area has demonstrated that the falling-stage and/or lowstand fluvial channel and the overlying transgressive estuarine fill are contained within a regionally developed incised valley (named Linxing paleovalley; Figure S1b) which developed during the previous fall in relative sea level [42].

Based on the aforementioned insights, the western coast of the early Gzhelian North China epeiric sea evolved from a mixed-energy barrier estuary with a fluvial-dominated and tide-influenced inner estuary in the HFC-2 and 3, through a tide-dominated estuary in the HFC-4, to a wave-dominated barrier lagoon in the HFC-5 to 7 in response to the interim relative sea-level rise. The coastal evolution from fluvial- through tide- to wave-dominated deposition in response to the relative sea-level rise in the study area is most common where an epicontinental or intracratonic coastal-plain incised valley formed during the previous sea-level fall is backfilled with transgressive inshore deposits. The Late Cretaceous Western Interior Seaway of North America changed from tide-dominated sheltered bay to wave-dominated open coasts during the relative sea-level rise [97]. The upper McMurray Formation, Grouse paleovalley, north-east Alberta, Canada, preserves a transgressive coastal depositional evolution from tide dominance with notable fluvial influence to wave dominance [98]. The Permian Rio Bonito Formation in the southern Paraná cratonic basin records the evolution of a fluvial- and tide-dominated estuarine valley to a wave-dominated barrier lagoon during a transgressive event [99].

In the study area, the funnel-shaped Linxing paleovalley coupled with an increased tidal prism induced by the upstepping and backstepping shoreline (Figure 2) contributed to the enhancement of tidal currents in the newly created estuary cf. [100], which resulted in the transition of the falling-stage and/or lowstand fluvial channels in HFC-1 into fluvial-dominated and tide-influenced inner estuaries in HFC-2 and 3 and then tide-dominated estuaries in HFC-4 (Figure S1a,b). The landward stepwise translation of tidal–fluvial channels led to significant incision (tidal and/or fluvial ravinement) within the estuary (Figure S1a,b). There is good potential for the preservation of the relatively coarse-grained tidal–fluvial channel and bar complexes backfilling the Linxing paleovalley as shown in Figure S1a,b. Because of its low gradient and cratonic setting, the western coast of the early Gzhelian North China epeiric sea was particularly sensitive to even small fluctuations in relative sea level. After the Linxing paleovalley was filled to the original interfluvial level in the southern Kangning, Tuban, and northwestern Sanjiaobei blocks (Figure S1a,b), the wide North China epeiric seaway lacking local coastline irregularities supplied sufficient fetch to large storm waves cf. [101,102], which led to the conversion of the tide-dominated estuaries in HFC-4 into the southwestward retrograding wave-dominated barrier lagoons in HFC-5 to 7. The turnaround from the transgressive to regressive shoreline trajectory is observed to be located in the northwestern Sanjiaobei block adjoining the southern Tuban block (i.e., between wells SJB-03 and TB-02 in cross-section A–A'; Figures 2 and S1a).

4.3. Grain-Size Distributions and Depositional Processes

4.3.1. Frequency Distribution Curves

The frequency distribution curves of the transgressive estuarine to lagoonal (FA1 to FA7) deposits from cores TB-01, 02, 03, and LX-8 show two pronounced peaks on both sides of the boundary between sand and mud (i.e., silt + clay) size fractions (Figure 7a–g). This indicates that FA1 to FA7 deposits are composed dominantly of sand and mud populations. The cumulative frequency distribution curves of FA1 to FA7 deposits illustrate a steep coarser-grained segment and a gently sloping, finer-grained segment (Figure 7h). The smooth transition between the two segments is interpreted to represent a mixture of two

overlapping normal populations [41,103]. Once sediment particles have been entrained and put into motion, they can be transported in two modes, bedload and suspended load [29,38,104,105]. Therefore, the coarser- and finer-grained segments substantially corresponding to the sand and mud populations are interpreted to have been transported prior to deposition by bedload and suspended load, respectively.

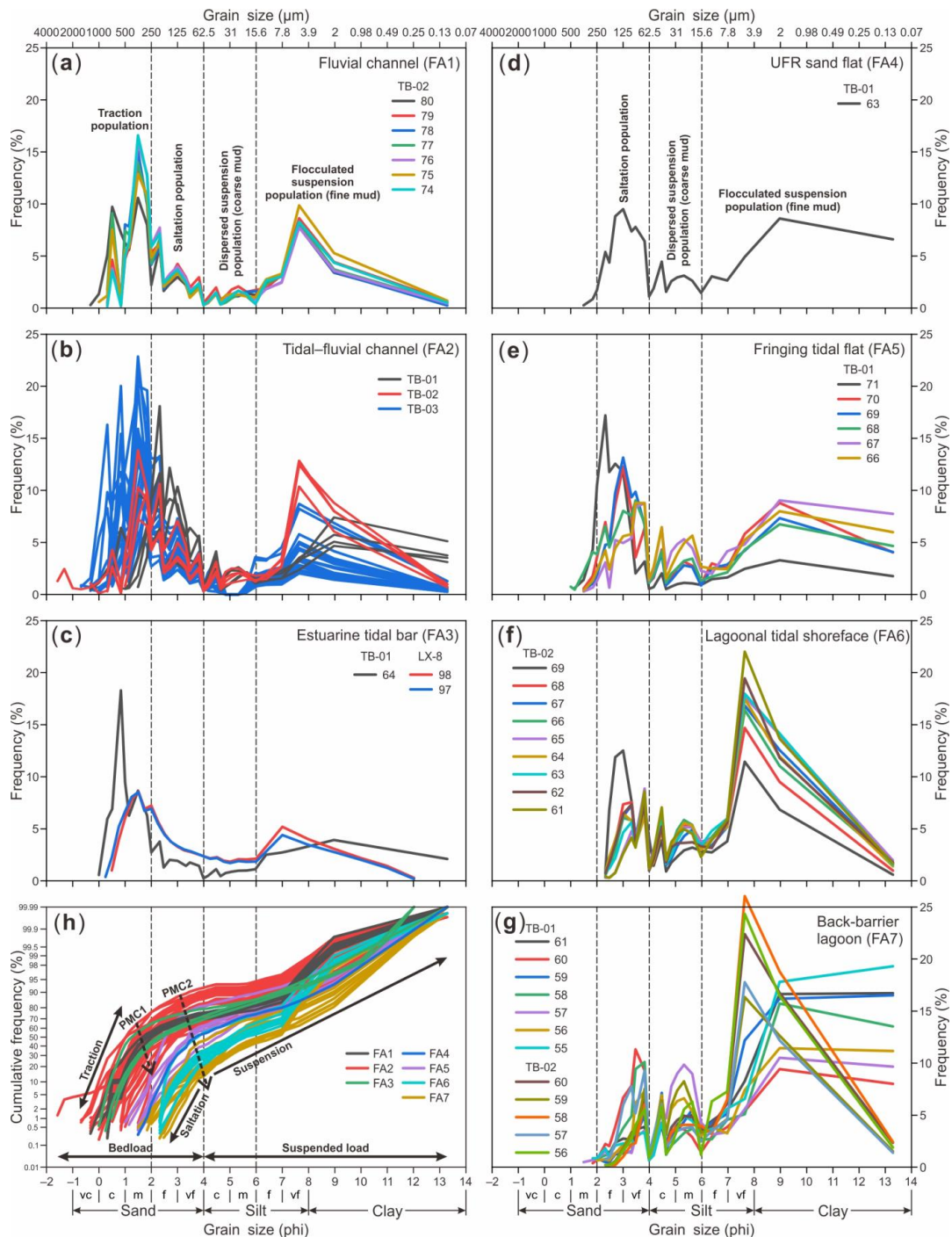


Figure 7. Frequency distribution curves (a–g) and cumulative frequency distribution curves (h) of transgressive estuarine to lagoonal deposits from cores TB-01, 02, 03, and LX-8. Altogether, four grain-size populations can be recognized on the polymodal distributions, interpreted as traction, saltation, dispersed suspension, and flocculated suspension populations from coarse to fine modes, respectively. The dashed lines mark the limit of the four populations. Abbreviation: vc—very coarse; c—coarse; m—medium; f—fine; vf—very fine; PMC—point of maximum curvature.

The bedload sand populations of FA1 to FA3 deposits mainly contain poorly sorted coarse to very fine sand particles with a modal size of dominantly medium sand (Figure 7a–c). The bedload sand populations of FA4 to FA7 deposits comprise predominantly well-sorted fine to very fine sand particles (Figure 7d–g). Process-based studies suggest that the coarser- and finer-grained fractions of the bedload population are commonly related to traction and saltation transport, respectively [9,106,107]. Therefore, the fine to very fine sand population of FA4 to FA7 deposits are interpreted to have been transported prior to deposition by saltation, whereas the coarse to very fine sand population of FA1 to FA3 deposits are interpreted to have been transported prior to deposition by mixed traction and saltation. The boundary between the traction and saltation populations is observed to be around 2 phi (Figure 7a–c,h), in accordance with the 2 phi proposed by Fuller [108].

The frequency distribution curves in Figure 7a–g show that the suspended load mud populations of FA1 to FA7 deposits consist of a dominantly coarse mud (coarse to medium silt) sub-population and a dominantly fine mud (fine silt to clay) sub-population. Process-based studies suggest that the coarser- and finer-grained fractions of the suspended load population are commonly related to dispersed and flocculated suspension transport, respectively [9,109–112]. Therefore, the coarse and fine mud sub-populations of FA1 to FA7 deposits are interpreted to have been transported prior to deposition by dispersed and flocculated suspensions, respectively. The flocculated suspension sub-populations (i.e., cohesive silts and clays) inevitably destroyed during sample preparation are interpreted to have been hydraulically equivalent to the dispersed suspension sub-populations (i.e., non-cohesive silts [113]). The transition from the dispersed to flocculated suspension sub-population is observed to be around 6 phi (15.6 μm), coarser than the 8–10 μm suggested by McCave et al. [114] and Chang, Flemming, and Bartholomä [113], but finer than the 20–22 μm proposed by Molinaroli, Guerzoni, De Falco, Sarretta, Cucco, Como, Simeone, Perilli and Magni [25] and Yawar and Schieber [115].

4.3.2. Ternary Diagram

To illustrate the overall grain-size compositional trends of the transgressive estuarine to lagoonal (FA1 to FA7) deposits from cores TB-01, 02, 03, and LX-8, the ternary diagrams with percentages of sand, coarse mud (coarse to medium silt), and fine mud (fine silt to clay) as end members are drawn to scale (Figure 8a–d); refer to Table S1 for detailed percentages of sand, coarse mud, and fine mud. The grain-size ranges of the sand, coarse mud, and fine mud fractions in these ternary diagrams precisely correspond to those of the bedload (i.e., sand), dispersed suspension (i.e., coarse to medium silt), and flocculated suspension (i.e., fine silt to clay) populations interpreted in the frequency distribution curves (Figure 7a–g). Therefore, the ternary diagrams in Figure 8a–d actually demonstrate the sediment dynamic compositional trends and the relative importance of bedload, dispersed suspension, and flocculated suspension populations in the development of FA1 to FA7 or their component lithofacies units.

The ternary diagram in Figure 8a shows that the overall grain-size compositional trend of FA1 to FA7 deposits from cores TB-01, 02, 03, and LX-8 are represented by a data band around the 2/3 partitioning of coarse and fine muds extending across the entire spectrum of lithofacies from sandstone through muddy sandstone and sandy mudstone to medium mudstone. The progression of the data band reveals the variation of dynamic sediment processes of FA1 to FA7 deposits from bedload- to suspended load-dominated, on the one hand, and between dispersed and flocculated suspensions, on the other. The ratios of dispersed suspended coarse mud to flocculated-suspended fine mud populations for FA1 to FA7 deposits are observed to be substantially around 2/3, mainly with more than 2/3 for the UFR sand flat (FA4) and fringing tidal flat (FA5) deposits and less than 2/3 for the fluvial channel (FA1) and tidal–fluvial channel (FA2) deposits (Figure 8a).

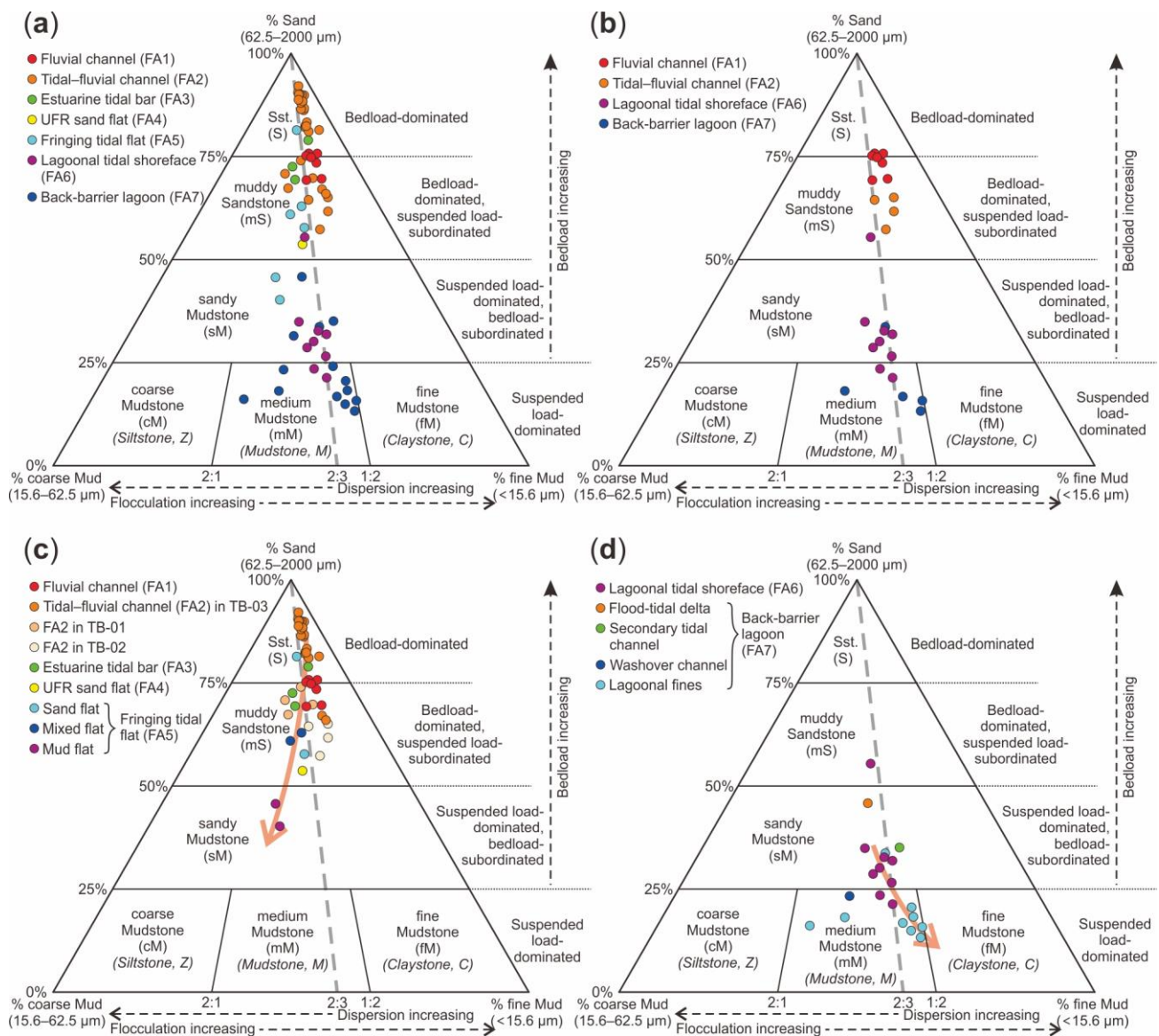


Figure 8. Ternary diagrams of transgressive estuarine to lagoonal deposits based on sand/coarse mud/fine mud ratios with cut-off between coarse and fine mud set at 15.6 µm. Boundary lines define different sediment textural types, as in Lazar, Bohacs, Macquaker, Schieber, and Demko [57]. (a) Transgressive estuarine to lagoonal samples from cores TB-01, 02, 03, and LX-8. (b) Transgressive estuarine to lagoonal samples from core TB-02. (c) Transgressive estuarine samples from cores TB-01, 02, 03, and LX-8. (d) Transgressive lagoonal samples from cores TB-01 and 02. The arrows in Figure 8c,d indicate the overall sediment dynamic trends.

Both the grain-size compositional ternary diagram (Figure 8b) and graphic log (Figure 3) for core TB-02 exhibit an overall decreasing bedload population from the fluvial channel (FA1) through the tidal–fluvial channel (FA2) and lagoonal tidal shoreface (FA6) to the back-barrier lagoon (FA7), in which there is a grain-size compositional gap between FA2 and FA6. This gap marks an abrupt change in sediment dynamic processes from bedload-dominated and suspended load-subordinated muddy sandstones (i.e., samples 73 to 70 in Figure 3) to suspended load-dominated and bedload-subordinated sandy mudstones (i.e., samples 69 to 61 in Figure 3) across a bay-ravinement surface (5BRS). Comparing the frequency distribution curves of FA2 and FA6 deposits from core TB-02 reveals that the bedload population has correspondingly transformed from mixed traction- and saltation-

dominated coarse to very fine sand populations into saltation-dominated fine to very fine sand populations across the 5BRS (Figure 7b,f).

The ternary diagram in Figure 8c combined with the cross-section B–B' in Figure S1b illustrates that the bedload-dominated sandstones (i.e., samples 39 to 18 in Figure 4) of the deeper tidal–fluvial channel (FA2) in core TB-03 pass eastward into the bedload-dominated and suspended load-subordinated muddy sandstones (i.e., samples 73, 72, 65 and 62 in Figure 5) of the shallower tidal–fluvial channel (FA2) followed by the bedload-dominated sandstones (i.e., sand flat sample 71 in Figure 5), bedload-dominated and suspended load-subordinated muddy sandstones (i.e., mixed flat samples 69 and 68 in Figure 5), and suspended load-dominated and bedload-subordinated sandy mudstones (i.e., mud flat samples 67 and 66 in Figure 5) of the fringing tidal flat (FA5) in core TB-01. Meanwhile, the bedload population has correspondingly changed from traction-dominated and saltation-subordinated in the deeper tidal–fluvial channel (FA2) to saltation-dominated and traction-subordinated in the shallower tidal–fluvial channel (FA2) and saltation-dominated in the fringing tidal flat (FA5). The grain-size breaks between FA2 and FA5 (Figure 7b,e) reflect the traction population confined within the channel. The suspension population correspondingly exhibits a progressively increasing dispersion/flocculation ratio from the deeper tidal–fluvial channel (FA2 in core TB-03) through the shallower tidal–fluvial channel (FA2 in core TB-01) to the fringing sand, mixed, and mud flats (FA5 in core TB-01; Figure 8c). Moreover, FA2 deposits (i.e., samples 73 to 70 in Figure 3) from core TB-02 have higher percentage of the suspension population than those of the fluvial channel (FA1) deposits (i.e., samples 80 to 74 in Figure 3) from core TB-02 and the estuarine tidal bar (FA3) deposits (i.e., sample 64 in Figure 5 and samples 98 and 97 in Figure 6) from cores TB-01 and LX-8. This is interpreted to have resulted from the presence of a bedload convergence showing the turbidity maximum within the tidal–fluvial channel [14].

The ternary diagram in Figure 8d shows that sediment dynamic processes of the lagoonal tidal shoreface (FA6) and back-barrier lagoon (FA7) deposits from cores TB-01 and 02 range from suspended load-dominated and bedload-subordinated to suspended load-dominated. The frequency distribution curves in Figure 7f,g show that the bedload population is exclusively composed of the saltation population. Data points of FA6 deposits (i.e., samples 69 to 61 in Figure 3) fall in the suspended load-dominated and saltation-subordinated sandy mudstone to suspended load-dominated medium mudstone field (Figure 8d). Data points of the flood-tidal delta (i.e., sample 62 in Figure 5) and secondary tidal channel deposits (i.e., sample 58 in Figure 5) of FA7 fall in the suspended load-dominated and saltation-subordinated sandy mudstone field. Data points of the washover channel (i.e., sample 56 in Figure 5) and lagoonal fine deposits (i.e., samples 61, 59, 57, and 55 in Figure 5 and samples 60, 59, 58, and 56 in Figure 3) of FA7 mainly fall in the suspended load-dominated medium mudstone field. The suspension population exhibits an overall increasing flocculation/dispersion ratio from the lagoonal tidal shoreface (FA6) in core TB-02 to the back-barrier lagoonal fines of FA7 in cores TB-01 and 02 (Figure 8d). Both the higher saltation populations of the flood-tidal delta (i.e., sample 60 in Figure 5), secondary tidal channel (i.e., sample 58 in Figure 5), and lagoonal fine deposits (i.e., sample 57 in Figure 3) and the higher dispersion/flocculation ratios of the washover channel (i.e., sample 56 in Figure 5) and lagoonal fine deposits (i.e., sample 59 in Figure 3 and sample 57 in Figure 5) are interpreted to indicate local wave and/or tidal influences (Figure 8d).

5. Conclusions

Integrated facies, sequence stratigraphic, and grain-size analyses of the Ximing Sandstone-to-No. 9 Coal succession of the Taiyuan Formation in the Linxing gas field reveal depositional responses to the relative sea-level rise in the western coast of the early Gzhelian North China epeiric sea. Six major conclusions are obtained:

- (1) Eight facies associations are recognized in the Ximing Sandstone-to-No. 9 Coal succession, including fluvial channel (FA1), tidal–fluvial channel (FA2), estuarine tidal

- bar (FA3), UFR sand flat (FA4), fringing tidal flat (FA5), lagoonal tidal shoreface (FA6), back-barrier lagoon (FA7), and lagoonal coastal mire (FA8).
- (2) Seven high-frequency stratigraphic cycles (HFC-1 to 7) separated by fluvial-, tidal-, and bay-ravinement surfaces are identified in the Ximing Sandstone-to-No. 9 Coal succession. HFC-1 consists predominantly of falling-stage and/or lowstand fluvial channel deposits (FA1). HFC-2 to 7 are stacked vertically to form a retrogradational succession that reflects evolution from barrier-fronted, fluvial-dominated, and tide-influenced inner estuaries (FA1 to FA3, FA5) in HFC-2 and 3 through tide-dominated estuaries (FA1 to FA5) in HFC-4 to wave-dominated barrier lagoons (FA6 to FA8) in HFC-5 to 7. The transgressive estuarine to lagoonal deposits accumulated below a wave-ravinement surface (WRS) but above a transgressively modified maximum regressive surface (MRS).
 - (3) The funnel-shaped Linxing paleovalley coupled with an increased tidal prism induced by the upstepping and backstepping shoreline contributed to the enhancement of tidal currents in the newly created estuary and led to the transition of the falling-stage and/or lowstand fluvial channel in HFC-1 into a fluvial-dominated and tide-influenced inner estuary in HFC-2 and 3 and then a tide-dominated estuary in HFC-4.
 - (4) The wide North China epeiric seaway lacking local coastline irregularities after the Linxing paleovalley fill supplied sufficient fetch to large storm waves, which led to the conversion of the tide-dominated estuary in HFC-4 into a southwestward retrograding wave-dominated barrier lagoon in HFC-5 to 7.
 - (5) The incised-valley estuary exhibits a sediment dynamic change from traction-dominated in the deeper tidal–fluvial channel through mixed traction- and saltation-dominated and suspension-subordinated in the shallower tidal–fluvial channel to saltation-dominated in the sand flat, saltation-dominated and suspension-subordinated in the mixed flat, and suspension-dominated and saltation-subordinated in the mud flat. The suspension population exhibits a progressively increasing dispersion/flocculation ratio along this sediment routing system.
 - (6) The wave-dominated barrier lagoon shows a sediment dynamic transition from suspended load-dominated and saltation-subordinated in the lagoonal tidal shoreface to suspended load-dominated in the back-barrier lagoon, in which the suspension population correspondingly shows a gradually increasing flocculation/dispersion ratio.

The combination of natural phenomena such as coastal erosion and pressures caused by human activities seriously threatens the protection of the present coastal environment. The study of coastal sedimentary dynamics is of strategic importance for the correct and sustainable territorial planning and utilization of coastal areas. The sea-level rise induced by ongoing global warming is rapidly altering the modern coastal environment. The prediction of recent coastal morpho-, hydro- and sediment dynamic processes based on the geological case study on coastal depositional responses to relative sea-level rise is another breakthrough research topic for the near future.

Supplementary Materials: The following supporting information can be downloaded at: <https://www.mdpi.com/article/10.3390/en16104144/s1>, Figure S1: (a) Cross-section A–A' along the length of the Linxing paleovalley. Note that the datum for wells SJB-03 through LX-8 is the composite surface at the top of the Linxing paleovalley fill, whereas the datum for well LX-8 through Palougou section is the WRS/MRS; (b) Cross-section B–B' approximately perpendicular to the length of the Linxing paleovalley. Note that the datum is the composite surface capping both the Linxing paleovalley fill and the interfluves. See Figure 2 for the tracks of cross-sections. Abbreviations: FSST—falling-stage systems tract; LST—lowstand systems tract; RST—regressive systems tract; TST—transgressive systems tract; Table S1: Grain-size parameters of transgressive estuarine to lagoonal deposits from cores TB-01, 02, 03, and LX-8.

Author Contributions: Conceptualization, J.L.; methodology, J.L.; investigation, J.L. and Y.Z.; data curation, J.L. and Y.Z.; writing—original draft preparation, J.L.; writing—review and editing, J.L. and

Y.Z.; visualization, J.L.; supervision, J.T.; funding acquisition, J.L. and J.T. All authors have read and agreed to the published version of the manuscript.

Funding: This research was funded by the Hunan Provincial Natural Science Foundation of China, grant number 2021JJ40724, Department of Natural Resources of Hunan Province (2022-5), and the China Hunan Provincial Science & Technology Department, grant number 2022WK2004.

Data Availability Statement: The data presented in this study are available on request from the corresponding author.

Acknowledgments: The authors are very grateful to the China United Coalbed Methane Corporation Limited for the data support.

Conflicts of Interest: The authors declare no conflict of interest. The funders had no role in the design of the study; in the collection, analyses, or interpretation of data; in the writing of the manuscript; or in the decision to publish the results.

References

1. Cowell, P.J.; Thom, B.G. Morphodynamics of coastal evolution. In *Coastal Evolution: Late Quaternary Shoreline Morphodynamics*; Carter, R.W.G., Woodroffe, C.D., Eds.; Cambridge University Press: Cambridge, UK, 1994; pp. 33–86.
2. Wright, L.D.; Thom, B.G. Coastal depositional landforms: A morphodynamic approach. *Prog. Phys. Geogr.* **1977**, *1*, 412–459. [[CrossRef](#)]
3. Miall, A.D. Sequence stratigraphy and geologic time. In *Stratigraphy & Timescales, Volume 2: Advances in Sequence Stratigraphy*; Montenari, M., Ed.; Academic Press: Cambridge, UK, 2017; pp. 59–83.S.
4. Catuneanu, O. Scale in sequence stratigraphy. *Mar. Pet. Geol.* **2019**, *106*, 128–159. [[CrossRef](#)]
5. Miall, A.D.; Holbrook, J.M.; Bhattacharya, J.P. The stratigraphy machine. *J. Sediment. Res.* **2021**, *91*, 595–610. [[CrossRef](#)]
6. Catuneanu, O.; Zecchin, M. High-resolution sequence stratigraphy of clastic shelves II: Controls on sequence development. *Mar. Pet. Geol.* **2013**, *39*, 26–38. [[CrossRef](#)]
7. Dalrymple, R.W. Introduction to siliciclastic facies models. In *Facies Models 4*; James, N.P., Dalrymple, R.W., Eds.; Geological Association of Canada: St. Johns, NL, Canada, 2010; pp. 59–72.
8. Miall, A.D. *The Geology of Stratigraphic Sequences*; Springer: Berlin, Germany, 2010; p. 522.
9. Wang, P. Principles of sediment transport applicable in tidal environments. In *Principles of Tidal Sedimentology*; Davis, R.A., Jr., Dalrymple, R.W., Eds.; Springer: Dordrecht, The Netherlands, 2012; pp. 19–34.
10. Nichols, M.M.; Boon, J.D. Sediment transport processes in coastal lagoons. In *Coastal Lagoon Processes*; Kjerfve, B., Ed.; Elsevier: Amsterdam, The Netherlands, 1994; pp. 157–219.
11. Dyer, K.R. Estuarine sediment transport and deposition. In *Sediment Transport and Depositional Processes*; Pye, K., Ed.; Blackwell Scientific Publications: London, UK, 1994; pp. 193–218.
12. Dyer, K.R. Sediment transport processes in estuaries. In *Geomorphology and Sedimentology of Estuaries*; Perillo, G.M.E., Ed.; Elsevier: Amsterdam, The Netherlands, 1995; pp. 423–449.
13. Dalrymple, R.W.; Choi, K. Morphologic and facies trends through the fluvial–marine transition in tide-dominated depositional systems: A schematic framework for environmental and sequence-stratigraphic interpretation. *Earth-Sci. Rev.* **2007**, *81*, 135–174. [[CrossRef](#)]
14. Dalrymple, R.W.; Mackay, D.A.; Ichaso, A.A.; Choi, K.S. Processes, morphodynamics, and facies of tide-dominated estuaries. In *Principles of Tidal Sedimentology*; Davis, R.A., Jr., Dalrymple, R.W., Eds.; Springer: Dordrecht, The Netherlands, 2012; pp. 79–107.
15. Wells, J.T. Tide-dominated estuaries and tidal rivers. In *Geomorphology and Sedimentology of Estuaries*; Perillo, G.M.E., Ed.; Elsevier: Amsterdam, The Netherlands, 1995; pp. 179–205.
16. Ainsworth, R.B.; Vakarelov, B.K.; Nanson, R.A. Dynamic spatial and temporal prediction of changes in depositional processes on clastic shorelines: Toward improved subsurface uncertainty reduction and management. *AAPG Bull.* **2011**, *95*, 267–297. [[CrossRef](#)]
17. Lambiase, J.J. Hydraulic control of grain-size distributions in a macrotidal estuary. *Sedimentology* **1980**, *27*, 433–446. [[CrossRef](#)]
18. Lambiase, J.J. Sediment dynamics in the macrotidal Avon River estuary, Bay of Fundy, Nova Scotia. *Can. J. Earth Sci.* **1980**, *17*, 1628–1641. [[CrossRef](#)]
19. Dalrymple, R.W.; Knight, R.J.; Zaitlin, B.A.; Middleton, G.V. Dynamics and facies model of a macrotidal sand-bar complex, Cobequid Bay–Salmon River Estuary (Bay of Fundy). *Sedimentology* **1990**, *37*, 577–612. [[CrossRef](#)]
20. Franz, G.; Pinto, L.; Ascione, I.; Mateus, M.; Fernandes, R.; Leitão, P.; Neves, R. Modelling of cohesive sediment dynamics in tidal estuarine systems: Case study of Tagus estuary, Portugal. *Estuar. Coast. Shelf Sci.* **2014**, *151*, 34–44. [[CrossRef](#)]
21. Carbajal, N.; Ley, Y.M.; Osuna, F.P.; Macías, M.D.J.G. Sediment dynamics in altata ensenada del pabellón, a coastal lagoon located in the Gulf of California. *J. Coast. Conserv.* **2018**, *22*, 709–720. [[CrossRef](#)]
22. Petti, M.; Bosa, S.; Pascolo, S. Lagoon sediment dynamics: A coupled model to study a medium-term silting of tidal channels. *Water* **2018**, *10*, 569. [[CrossRef](#)]
23. Flemming, B.W. Particle shape-controlled sorting and transport behaviour of mixed siliciclastic/bioclastic sediments in a mesotidal lagoon, South Africa. *Geo-Mar. Lett.* **2017**, *37*, 397–410. [[CrossRef](#)]

24. Montaña-Ley, Y.; Carbajal, N.; Páez-Osuna, F. Sediment dynamics in a complex coastal lagoon system of the Gulf of California. *J. Coast. Conserv.* **2015**, *19*, 295–306. [[CrossRef](#)]
25. Molinaroli, E.; Guerzoni, S.; De Falco, G.; Sarretta, A.; Cucco, A.; Como, S.; Simeone, S.; Perilli, A.; Magni, P. Relationships between hydrodynamic parameters and grain size in two contrasting transitional environments: The Lagoons of Venice and Cabras, Italy. *Sediment. Geol.* **2009**, *219*, 196–207. [[CrossRef](#)]
26. Bortolin, E.C.; Weschenfelder, J.; Fernandes, E.H.; Bitencourt, L.P.; Möller, O.O.; García-Rodríguez, F.; Toldo, E. Reviewing sedimentological and hydrodynamic data of large shallow coastal lagoons for defining mud depocenters as environmental monitoring sites. *Sediment. Geol.* **2020**, *410*, 105782. [[CrossRef](#)]
27. Leitão, P.C.; Mateus, M.; Braunschweig, F.; Fernandes, L.; Neves, R. Modelling coastal systems: The MOHID water numerical lab. In *Perspectives on Integrated Coastal Zone Management in South America*; Neves, R., Baretta, J., Mateus, M., Eds.; IST Press: Lisbon, Portugal, 2008; pp. 77–88.
28. Pye, K. Properties of sediment particles. In *Sediment Transport and Depositional Processes*; Pye, K., Ed.; Blackwell Scientific Publications: London, UK, 1994; pp. 1–24.
29. Allen, P.A. *Earth Surface Processes*; John Wiley & Sons: Hoboken, NJ, USA, 1997.
30. Hartmann, D.; Flemming, B. From particle size to sediment dynamics: An introduction. *Sediment. Geol.* **2007**, *202*, 333–336. [[CrossRef](#)]
31. McLaren, P.; Bowles, D. The effects of sediment transport on grain-size distributions. *J. Sediment. Petrol.* **1985**, *55*, 457–470.
32. Visher, G.S. Grain size distributions and depositional processes. *J. Sediment. Petrol.* **1969**, *39*, 1074–1106.
33. Passega, R. Grain-size representation by CM patterns as a geological tool. *J. Sediment. Petrol.* **1964**, *34*, 830–847. [[CrossRef](#)]
34. McCave, I.N.; Syvitski, J.P.M. Principles and methods of geological particle size analysis. In *Principles, Methods and Application of Particle Size Analysis*; Syvitski, J.P.M., Ed.; Cambridge University Press: Cambridge, UK, 1991; pp. 3–21.
35. Xiao, J.; Chang, Z.; Fan, J.; Zhou, L.; Zhai, D.; Wen, R.; Qin, X. The link between grain-size components and depositional processes in a modern clastic lake. *Sedimentology* **2012**, *59*, 1050–1062. [[CrossRef](#)]
36. Gammon, P.R.; Neville, L.A.; Patterson, R.T.; Savard, M.M.; Swindles, G.T. A log-normal spectral analysis of inorganic grain-size distributions from a Canadian boreal lake core: Towards refining depositional process proxy data from high latitude lakes. *Sedimentology* **2017**, *64*, 609–630. [[CrossRef](#)]
37. Middleton, G.V. Hydraulic interpretation of sand size distributions. *J. Geol.* **1976**, *84*, 405–426. [[CrossRef](#)]
38. Middleton, G.V.; Southard, J.B. *Mechanics of Sediment Movement*; SEPM Short Course Notes No. 3; SEPM Society for Sedimentary Geology: Tulsa, OK, USA, 1984; p. 410.
39. Dalrymple, R.W. Sediment Dynamics of Macrotidal Sand Bars, Bay of Fundy. Unpublished. Ph.D. Thesis, McMaster University, Hamilton, ON, Canada, 1977.
40. Sun, D.; Bloemendal, J.; Rea, D.K.; Vandenberghe, J.; Jiang, F.; An, Z.; Su, R. Grain-size distribution function of polymodal sediments in hydraulic and aeolian environments, and numerical partitioning of the sedimentary components. *Sediment. Geol.* **2002**, *152*, 263–277. [[CrossRef](#)]
41. Viard, J.P.; Breyer, J.A. Description and hydraulic interpretation of grain size cumulative curves from the Platte River system. *Sedimentology* **1979**, *26*, 427–439. [[CrossRef](#)]
42. Liu, J.; Cao, D.; Zhang, Y.; Li, Y. Temporal changes in an epeiric paralic deposition during a third-order relative sea-level cycle (Late Pennsylvanian, western North China): Insights from integrated facies and sequence stratigraphic analysis. *J. Asian Earth Sci.* **2020**, *196*, 104349. [[CrossRef](#)]
43. Zhao, G.; Wang, Y.; Huang, B.; Dong, Y.; Li, S.; Zhang, G.; Yu, S. Geological reconstructions of the East Asian blocks: From the breakup of Rodinia to the assembly of Pangea. *Earth-Sci. Rev.* **2018**, *186*, 262–286. [[CrossRef](#)]
44. Ma, S.; Meng, Q.; Duan, L.; Wu, G. Reconstructing Late Paleozoic exhumation history of the Inner Mongolia Highland along the northern edge of the North China Craton. *J. Asian Earth Sci.* **2014**, *87*, 89–101. [[CrossRef](#)]
45. Haq, B.U.; Schutter, S.R. A chronology of Paleozoic sea-level changes. *Science* **2008**, *322*, 64–68. [[CrossRef](#)]
46. Zhang, H.; Shen, G.; He, Z. Control of palaeoclimatic change on Late Palaeozoic coal accumulation of the North China Plate. *Acta Geol. Sin.* **1999**, *73*, 131–139. (In Chinese with English Abstract)
47. Ma, S.; Meng, Q.; Wu, G.; Duan, L. Late Paleozoic exhumation of the Inner Mongolia Paleo-uplift: Evidences from sedimentary records. *Acta Geol. Sin.* **2014**, *88*, 1771–1789. (In Chinese with English Abstract)
48. Chen, Q.; Li, W.; Liu, H.; Li, K.; Pang, J.; Guo, Y.; Yuan, Z. Provenance analysis of sandstone of the Upper Carboniferous to Middle Permian in Ordos Basin. *J. Palaeogeogr.* **2009**, *11*, 629–640.
49. Chen, Q.; Li, W.; Hu, X.; Li, K.; Pang, J.; Guo, Y. Tectonic setting and provenance analysis of Late Paleozoic sedimentary rocks in the Ordos Basin. *Acta Geol. Sin.* **2012**, *86*, 1150–1162. (In Chinese with English Abstract)
50. Wu, F.; Zhang, N. Sequence stratigraphic analysis of Late Paleozoic coal-bearing measures in North China. In *The Depositional Environments and Coal-Accumulating Regularities of Late Paleozoic Coal-Bearing Measures in North China*; Chen, Z., Wu, F., Zhang, S., Zhang, N., Ma, J., Ge, L., Eds.; Press of China University of Geosciences: Wuhan, China, 1993; pp. 124–134. (In Chinese with English Abstract)
51. Wu, F.; Chen, Z.; Zhang, S.; Ge, L. Preliminary study on sequence stratigraphy of Late Paleozoic coal-bearing basin in North China. *Coal Geol. China* **1994**, *6*, 11–18. (In Chinese)

52. Wang, C.Y.; Kang, P.Q. The base of the Permian System in China. *Acta Micropalaeontol. Sin.* **2000**, *17*, 378–387. (In Chinese with English Abstract)
53. Wu, Q.; Ramezani, J.; Zhang, H.; Wang, J.; Zeng, F.; Zhang, Y.; Liu, F.; Chen, J.; Cai, Y.; Hou, Z.; et al. High-precision U-Pb age constraints on the Permian floral turnovers, paleoclimate change, and tectonics of the North China block. *Geology* **2021**, *49*, 677–681. [[CrossRef](#)]
54. Sun, B.; Zeng, F.; Liu, C.; Cui, X.; Wang, W. Constraints on U-Pb dating of detrital zircon of the maximum depositional age for Upper Paleozoic coal-bearing strata in Xishan, Taiyuan and its stratigraphic significance. *Acta Geol. Sin.* **2014**, *88*, 185–197. (In Chinese with English Abstract)
55. Liu, G. Permo-Carboniferous paleogeography and coal accumulation and their tectonic control in the North and South China continental plates. *Int. J. Coal Geol.* **1990**, *16*, 73–117. [[CrossRef](#)]
56. Jin, Y.; Shang, Q. The Permian of China and its interregional correlation. In *Permian-Triassic Evolution of Tethys and Western Circum-Pacific*; Yin, H., Dickinson, J.M., Shi, G.R., Tong, J., Eds.; Elsevier: Amsterdam, The Netherlands, 2000; pp. 71–98.
57. Lazar, O.R.; Bohacs, K.M.; Macquaker, J.H.S.; Schieber, J.; Demko, T.M. Capturing key attributes of fine-grained sedimentary rocks in outcrops, cores, and thin sections: Nomenclature and description guidelines. *J. Sediment. Res.* **2015**, *85*, 230–246. [[CrossRef](#)]
58. Dalrymple, R.W.; Zaitlin, B.A.; Boyd, R. Estuarine facies models: Conceptual basis and stratigraphic implications. *J. Sediment. Petrol.* **1992**, *62*, 1130–1146. [[CrossRef](#)]
59. Van den Berg, J.H.; Martinius, A.W.; Houthuys, R. Breaching-related turbidites in fluvial and estuarine channels: Examples from outcrop and core and implications to reservoir models. *Mar. Pet. Geol.* **2017**, *82*, 178–205. [[CrossRef](#)]
60. Rinke-Hardekopf, L.; Dashtgard, S.E.; MacEachern, J.A.; Gingras, M.K. Resolving stratigraphic architecture and constraining ages of paralic strata in a low-accommodation setting, Firebag Tributary, McMurray Formation, Canada. *Depos. Rec.* **2022**, *8*, 754–785. [[CrossRef](#)]
61. Shiers, M.N.; Mountney, N.P.; Hodgson, D.M.; Colombero, L. Controls on the depositional architecture of fluvial point-bar elements in a coastal-plain succession. In *Fluvial Meanders and Their Sedimentary Products in the Rock Record*; Ghinassi, M., Colombero, L., Mountney, N.P., Reesink, A.J.H., Eds.; International Association of Sedimentologists Special Publication 48; John Wiley & Sons, Inc.: Hoboken, NJ, USA, 2018; pp. 15–46.
62. Mutti, E.; Allen, G.P.; Rosell, J. Sigmoidal-cross stratification and sigmoidal bars: Depositional features diagnostic of tidal sandstones. In Proceedings of the 5th IAS European Regional Meeting, Marsiglia, France, 9–11 April 1984; pp. 312–313.
63. Tinterri, R. Combined flow sedimentary structures and the genetic link between sigmoidal-and hummocky-cross stratification. *GeoActa* **2011**, *10*, 43–85.
64. Ichaso, A.A.; Dalrymple, R.W. Tide- and wave-generated fluid mud deposits in the Tilje Formation (Jurassic), offshore Norway. *Geology* **2009**, *37*, 539–542. [[CrossRef](#)]
65. Miall, A.D. Alluvial deposits. In *Facies Models 4*; James, N.P., Dalrymple, R.W., Eds.; Geological Association of Canada GEOText 6: St. John's, NL, Canada, 2010; pp. 105–137.
66. Jablonski, B.V.J.; Dalrymple, R.W. Recognition of strong seasonality and climatic cyclicity in an ancient, fluvially dominated, tidally influenced point bar: Middle McMurray Formation, Lower Steepbank River, north-eastern Alberta, Canada. *Sedimentology* **2016**, *63*, 552–585. [[CrossRef](#)]
67. Choi, K. Tidal rhythmites in a mixed-energy, macrotidal estuarine channel, Gomso Bay, west coast of Korea. *Mar. Geol.* **2011**, *280*, 105–115. [[CrossRef](#)]
68. Pelletier, J.; Abouessa, A.; Schuster, M.; Durringer, P.; Rubino, J.L. Hierarchy of tidal rhythmites from semidiurnal to solstitial cycles: Origin of inclined heterolithic stratifications (IHS) in tidal channels from the Dur At Talah Formation (upper Eocene, Sirte Basin, Libya) and a facies comparison with modern Mont-Saint-Michel Bay deposits (France). In *Contributions to Modern and Ancient Tidal Sedimentology: Proceedings of the Tidalites 2012 Conference*; Tessier, B., Reynaud, J.-Y., Eds.; International Association of Sedimentologists, Special Publication 47; John Wiley & Sons, Inc.: Hoboken, NJ, USA, 2016; pp. 203–216.
69. Mackay, D.A.; Dalrymple, R.W. Dynamic mud deposition in a tidal environment: The record of fluid-mud deposition in the Cretaceous Bluesky Formation, Alberta, Canada. *J. Sediment. Res.* **2011**, *81*, 901–920. [[CrossRef](#)]
70. Choi, K. Rhythmic climbing-ripple cross-lamination in inclined heterolithic stratification (IHS) of a macrotidal estuarine channel, Gomso Bay, west coast of Korea. *J. Sediment. Res.* **2010**, *80*, 550–561. [[CrossRef](#)]
71. Dalrymple, R.W. Tidal depositional systems. In *Facies Models 4*, James, N.P., Dalrymple, R.W., Eds.; Geological Association of Canada GEOText 6: St. John's, NL, Canada, 2010; pp. 201–231.
72. Dalrymple, R.W.; Rhodes, R.N. Estuarine dunes and bars. In *Geomorphology and Sedimentology of Estuaries. Developments in Sedimentology*; Perillo, G.M.E., Ed.; Elsevier: Amsterdam, The Netherlands, 1995; Volume 53, pp. 359–422.
73. Fenies, H.; Tastet, J.-P. Facies and architecture of an estuarine tidal bar (the Trompeloup bar, Gironde Estuary, SW France). *Mar. Geol.* **1998**, *150*, 149–169. [[CrossRef](#)]
74. Allen, G.P.; Posamentier, H.W. Sequence stratigraphy and facies model of an incised valley fill: The Gironde Estuary, France. *J. Sediment. Petrol.* **1993**, *63*, 378–391.
75. Allen, G.P. Sedimentary processes and facies in the Gironde estuary: A recent model for macrotidal estuarine systems. In *Clastic Tidal Sedimentology*; Smith, D.G., Reinson, G.E., Zaitlin, B.A., Rahmani, R.A., Eds.; Canadian Society of Petroleum Geologists Memoir 16: Calgary, AB, Canada, 1991; pp. 29–40.
76. Dalrymple, R.W. Morphology and internal structure of sandwaves in the Bay of Fundy. *Sedimentology* **1984**, *31*, 365–382. [[CrossRef](#)]

77. Olariu, C.; Steel, R.J.; Dalrymple, R.W.; Gingras, M.K. Tidal dunes versus tidal bars: The sedimentological and architectural characteristics of compound dunes in a tidal seaway, the lower Baronia Sandstone (Lower Eocene), Ager Basin, Spain. *Sediment. Geol.* **2012**, *279*, 134–155. [[CrossRef](#)]
78. Dashtgard, S.E.; Gingras, M.K. Facies architecture and ichnology of recent salt-marsh deposits: Waterside Marsh, New Brunswick, Canada. *J. Sediment. Res.* **2005**, *75*, 596–607. [[CrossRef](#)]
79. Dalrymple, R.W.; Makino, Y.; Zaitlin, B.A. Temporal and spatial patterns of rhythmite deposition on mud flats in the macrotidal Cobequid Bay-Salmon River estuary, Bay of Fundy, Canada. In *Clastic Tidal Sedimentology*; Smith, D.G., Reinson, G.E., Zaitlin, B.A., Rahmani, R.A., Eds.; Canadian Society of Petroleum Geologists, Memoir 16: Calgary, AB, Canada, 1991; pp. 137–160.
80. Iseya, F. A depositional process of reverse graded bedding in flood deposits of the Sakura River, Ibaraki Prefecture, Japan. *Geogr. Rev. Jpn.* **1982**, *55*, 597–613. [[CrossRef](#)]
81. Masuda, F.; Iseya, F. “Inverse grading”: A facies structure of flood deposits in meandering rivers. *J. Sedimentol. Soc. Jpn.* **1985**, *22*, 108–116.
82. Fan, D. Classifications, sedimentary features and facies associations of tidal flats. *J. Palaeogeogr.* **2013**, *2*, 66–80.
83. Dashtgard, S.E.; Vaucher, R.; Yang, B.; Dalrymple, R.W. Hutchison Medallist 1. Wave-Dominated to Tide-Dominated Coastal Systems: A Unifying Model for Tidal Shorefaces and Refinement of the Coastal-Environments Classification Scheme. *Geosci. Can.* **2021**, *48*, 5–22. [[CrossRef](#)]
84. de Raaf, J.F.M.; Boersma, J.R.; van Gelder, A. Wave-generated structures and sequences from a shallow marine succession, Lower Carboniferous, County Cork, Ireland. *Sedimentology* **1977**, *24*, 451–483. [[CrossRef](#)]
85. Plint, A.G. Wave- and storm-dominated shoreline and shallow-marine systems. In *Facies Models 4*; James, N.P., Dalrymple, R.W., Eds.; Geological Association of Canada GEOText 6: St. John’s, NL, Canada, 2010; pp. 167–200.
86. Allen, J.L.; Johnson, C.L. Architecture and formation of transgressive–regressive cycles in marginal marine strata of the John Henry Member, Straight Cliffs Formation, Upper Cretaceous of Southern Utah, USA. *Sedimentology* **2011**, *58*, 1486–1513. [[CrossRef](#)]
87. Olsen, T.R.; Mellere, D.; Olsen, T. Facies architecture and geometry of landward-stepping shoreface tongues: The Upper Cretaceous Cliff House Sandstone (Mancos Canyon, south-west Colorado). *Sedimentology* **1999**, *46*, 603–625. [[CrossRef](#)]
88. Chentnik, B.M.; Johnson, C.L.; Mulhern, J.S.; Stright, L. Valleys, estuaries, and lagoons: Paleoenvironments and regressive–transgressive architecture of the Upper Cretaceous Straight Cliffs Formation, Utah, USA. *J. Sediment. Res.* **2015**, *85*, 1166–1196. [[CrossRef](#)]
89. Bridges, P.H. Lower Silurian transgressive barrier islands, southwest Wales. *Sedimentology* **1976**, *23*, 347–362. [[CrossRef](#)]
90. Schwartz, R.K. Bedform and stratification characteristics of some modern small-scale washover sand bodies. *Sedimentology* **1982**, *29*, 835–849. [[CrossRef](#)]
91. Noe-Nygaard, N.; Surlyk, F. Washover fan and brackish bay sedimentation in the Berriasian-Valanginian of Bornholm, Denmark. *Sedimentology* **1988**, *35*, 197–217. [[CrossRef](#)]
92. Donselaar, M.E.; Nio, S.D. An Eocene tidal inlet/washover type barrier island complex in the South Pyrenean marginal basin, Spain. *Geol. En Mijnb.* **1982**, *61*, 343–353.
93. Blum, M.; Martin, J.; Milliken, K.; Garvin, M. Paleovalley systems: Insights from Quaternary analogs and experiments. *Earth-Sci. Rev.* **2013**, *116*, 128–169. [[CrossRef](#)]
94. Boyd, R.; Dalrymple, R.W.; Zaitlin, B.A. Estuarine and incised-valley facies models. In *Facies Models Revisited*; Posamentier, H.W., Walker, R.G., Eds.; SEPM Special Publication 84; SEPM Society for Sedimentary Geology: Tulsa, OK, USA, 2006; pp. 171–235.
95. Reinson, G.E. Transgressive barrier island and estuarine systems. In *Facies Models: Response to Sea Level Change*; Walker, R.G., James, N.P., Eds.; Geological Association of Canada: St. John’s, NL, Canada, 1992; pp. 179–194.
96. Boyd, R. Transgressive wave-dominated coasts. In *Facies Models 4*; James, N.P., Dalrymple, R.W., Eds.; Geological Association of Canada GEOText 6: St. John’s, NL, Canada, 2010; pp. 265–294.
97. Yoshida, S.; Steel, R.J.; Dalrymple, R.W. Changes in depositional processes—An ingredient in a new generation of sequence-stratigraphic models. *J. Sediment. Res.* **2007**, *77*, 447–460. [[CrossRef](#)]
98. Weleschuk, Z.P.; Dashtgard, S.E. Evolution of an ancient (Lower Cretaceous) marginal-marine system from tide-dominated to wave-dominated deposition, McMurray Formation. *Sedimentology* **2019**, *66*, 2354–2391. [[CrossRef](#)]
99. Galli, C.P.; Cagliari, J.; Lavina, E.L.C. Evolution of an estuarine valley to barrier-lagoon system promoted by tidal prism change during a transgressive event (Lower Permian, Paraná Basin). *J. South Am. Earth Sci.* **2021**, *110*, 103398. [[CrossRef](#)]
100. Tessier, B. Stratigraphy of tide-dominated estuaries. In *Principles of Tidal Sedimentology*; Davis, R.A., Jr., Dalrymple, R.W., Eds.; Springer: Dordrecht, The Netherlands, 2012; pp. 109–128.
101. Ericksen, M.C.; Slingerland, R. Numerical simulations of tidal and wind-driven circulation in the Cretaceous Interior Seaway of North America. *Geol. Soc. Am. Bull.* **1990**, *102*, 1499–1516. [[CrossRef](#)]
102. Slingerland, R.L.; Keen, T.R. Sediment transport in the Western Interior Seaway of North America: Predictions from a climate-ocean-sediment model. In *Isolated Shallow Marine Sand Bodies: Sequence Stratigraphic Analysis and Sedimentologic Interpretation*; Bergman, K.M., Snedden, J.W., Eds.; SEPM Special Publication No. 64; SEPM Society for Sedimentary Geology: Tulsa, OK, USA, 1999; pp. 179–190.
103. Bein, A.; Sass, E. Analysis of log-probability plots of recent Atlantic sediments and its analogy with simulated mixtures. *Sedimentology* **1978**, *25*, 575–581. [[CrossRef](#)]
104. Inman, D.L. Sorting of sediments in the light of fluid mechanics. *J. Sediment. Petrol.* **1949**, *19*, 51–70.

105. Allen, J.R.L. Fundamental properties of fluids and their relation to sediment transport processes. In *Sediment Transport and Depositional Processes*; Pye, K., Ed.; Blackwell Scientific Publications: London, UK, 1994; pp. 25–60.
106. Singer, J.K.; Anderson, J.B. Use of total grain-size distributions to define bed erosion and transport for poorly sorted sediment undergoing simulated bioturbation. *Mar. Geol.* **1984**, *57*, 335–359. [[CrossRef](#)]
107. Bagnold, R.A. The nature of saltation and of ‘bed-load’ transport in water. *Proc. R. Soc. Lond. A* **1973**, *332*, 473–504.
108. Fuller, A.O. Size distribution characteristics of shallow marine sands from the Cape of Good Hope, South Africa. *J. Sediment. Petrol.* **1961**, *31*, 256–261. [[CrossRef](#)]
109. Dyer, K.R. *Coastal and Estuarine Sediment Dynamics*; John Wiley & Sons, Inc.: Chichester, UK, 1986; p. 342.
110. Whitehouse, R.; Soulsby, R.; Roberts, W.; Mitchener, H. *Dynamics of Estuarine Muds: A Manual for Practical Applications*; Thomas Telford Publishing: London, UK, 2000; p. 210.
111. Van Ledden, M.; Van Kesteren, W.G.M.; Winterwerp, J.C. A conceptual framework for the erosion behaviour of sand–mud mixtures. *Cont. Shelf Res.* **2004**, *24*, 1–11. [[CrossRef](#)]
112. Mikkelsen, O.; Pejrup, M. Comparison of flocculated and dispersed suspended sediment in the Dollard estuary. In *Sedimentary Processes in the Intertidal Zone*; Black, K.S., Paterson, D.M., Cramp, A., Eds.; Special Publication 139; Geological Society: London, UK, 1998; pp. 199–209.
113. Chang, T.S.; Flemming, B.W.; Bartholomä, A. Distinction between sortable silts and aggregated particles in muddy intertidal sediments of the East Frisian Wadden Sea, southern North Sea. *Sediment. Geol.* **2007**, *202*, 453–463. [[CrossRef](#)]
114. McCave, I.N.; Manighetti, B.; Robinson, S.G. Sortable silt and fine sediment size/composition slicing: Parameters for palaeocurrent speed and palaeoceanography. *Paleoceanography* **1995**, *10*, 593–610. [[CrossRef](#)]
115. Yawar, Z.; Schieber, J. On the origin of silt laminae in laminated shales. *Sediment. Geol.* **2017**, *360*, 22–34. [[CrossRef](#)]

Disclaimer/Publisher’s Note: The statements, opinions and data contained in all publications are solely those of the individual author(s) and contributor(s) and not of MDPI and/or the editor(s). MDPI and/or the editor(s) disclaim responsibility for any injury to people or property resulting from any ideas, methods, instructions or products referred to in the content.